



Published in final edited form as:

Cell Rep. 2024 January 23; 43(1): 113661. doi:10.1016/j.celrep.2023.113661.

VISTA promotes the metabolism and differentiation of myeloid-derived suppressor cells by STAT3 and polyamine-dependent mechanisms

Keman Zhang^{1,7}, Amin Zakeri^{1,7}, Tyler Alban^{2,7}, Juan Dong¹, Hieu M. Ta¹, Ajay H. Zalavadia³, Andrele Branicky³, Haoxin Zhao³, Ivan Juric², Hanna Husich², Prerana B. Parthasarathy², Amit Rupani², Judy A. Drazba³, Abhishek A. Chakraborty⁴, Stanley Ching-Cheng Huang^{5,6}, Timothy Chan², Stefanie Avril^{5,6}, Li Lily Wang^{1,8,*}

¹Department of Translational Hematology and Oncology Research, Cleveland Clinic Foundation, 9500 Euclid Avenue, Cleveland, OH, USA

²Center for Immunotherapy and Precision Immuno-Oncology, Cleveland Clinic Foundation, 9500 Euclid Avenue, Cleveland, OH, USA

³Imaging Core Facility, Cleveland Clinic Foundation, 9500 Euclid Avenue, Cleveland, OH, USA

⁴Department of Cancer Biology, Cleveland Clinic Foundation, 9500 Euclid Avenue, Cleveland, OH, USA

⁵Department of Pathology, University Hospitals Cleveland Medical Center, and Case Western Reserve University School of Medicine, Cleveland, OH, USA

⁶Case Comprehensive Cancer Center, Cleveland, OH, USA

⁷These authors contributed equally

⁸Lead contact

SUMMARY

Myeloid-derived suppressor cells (MDSCs) impair antitumor immune responses. Identifying regulatory circuits during MDSC development may bring new opportunities for therapeutic interventions. We report that the V-domain suppressor of T cell activation (VISTA) functions as a key enabler of MDSC differentiation. VISTA deficiency reduced STAT3 activation and STAT3-dependent production of polyamines, which causally impaired mitochondrial respiration and MDSC expansion. In both mixed bone marrow (BM) chimera mice and myeloid-specific VISTA

This is an open access article under the CC BY-NC-ND license (<http://creativecommons.org/licenses/by-nc-nd/4.0/>).

*Correspondence: wangl9@ccf.org.

AUTHOR CONTRIBUTIONS

Conceptualization, L.L.W.; methodology, K.Z., A.Z., T.A., J.D., H.M.T., A.H.Z., A.B., H.Z., I.J., H.H., P.B.P., A.R., J.A.D., A.A.C., S.C.-C.H., S.A., T.C., and T.A.; investigation, K.Z., A.Z., T.A., J.D., A.H.Z., A.B., H.Z., and S.A.; visualization, L.L.W., K.Z., A.Z., T.A., and I.J.; funding acquisition, L.L.W.; project administration, L.L.W.; supervision, L.L.W.; writing – original draft, L.L.W., K. Z., A.Z., and T.A.; writing – review & editing, L.L.W., K.Z., A.Z., T.A., S.C.-C.H., and S.A.

SUPPLEMENTAL INFORMATION

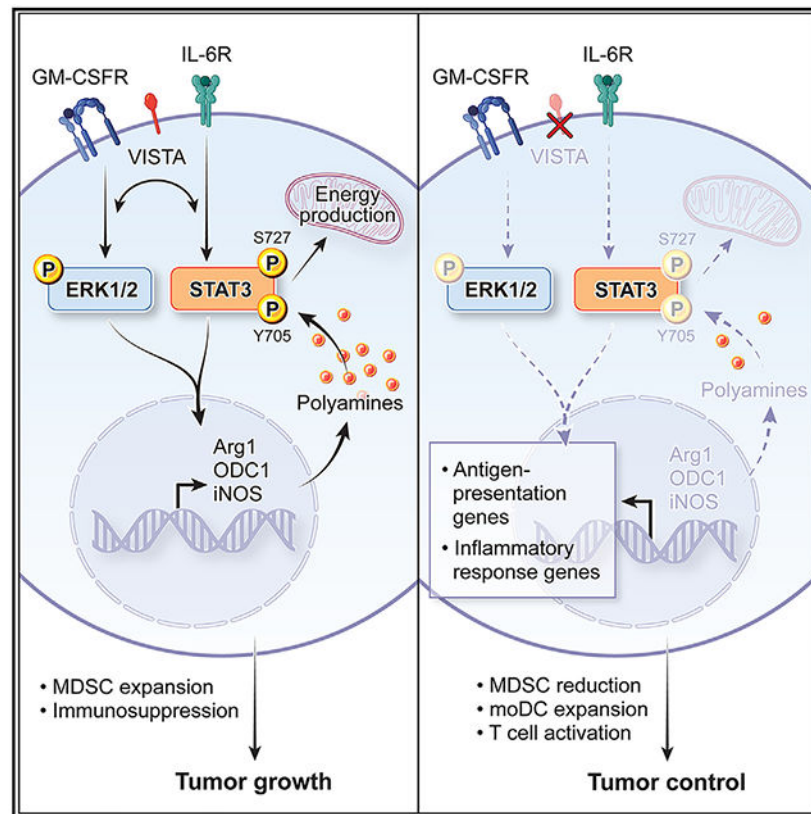
Supplemental information can be found online at <https://doi.org/10.1016/j.celrep.2023.113661>.

DECLARATION OF INTERESTS

L.L.W is an inventor involved with the commercial development of VISTA with ImmuNext Inc. Corporation (Lebanon, NH, USA).

conditional knockout mice, VISTA deficiency significantly reduced tumor-associated MDSCs but expanded monocyte-derived dendritic cells (DCs) and enhanced T cell-mediated tumor control. Correlated expression of VISTA and arginase-1 (ARG1), a key enzyme supporting polyamine biosynthesis, was observed in multiple human cancer types. In human endometrial cancer, co-expression of VISTA and ARG1 on tumor-associated myeloid cells is associated with poor survival. Taken together, these findings unveil the VISTA/polyamine axis as a central regulator of MDSC differentiation and warrant therapeutically targeting this axis for cancer immunotherapy.

Graphical Abstract



In brief

Zhang et al. have identified a causal role of an immune checkpoint protein, VISTA, in driving MDSC differentiation by promoting STAT3 activation, polyamine biosynthesis, and mitochondrial respiration. Blocking VISTA in monocytic progenitors reduced MDSCs and improved antitumor immunity. Correlated expression of VISTA and ARG1 is prognostic in human endometrial cancer.

INTRODUCTION

Myeloid-derived suppressor cells (MDSCs) impair anti-tumor immune responses and are often associated with a poor prognosis in cancer.¹⁻⁴ In humans and mice, MDSCs consist of two major subsets: monocytic MDSCs (M-MDSCs) morphologically and phenotypically resemble monocytes, with surface markers CD11b⁺ Ly6C^{hi} Ly6G⁻ in mice and CD11b⁺

CD14⁺ CD33⁺ HLA⁻ DR⁻ in humans, and polymorphonuclear (PMN)-MDSCs resemble neutrophils, with the surface markers CD11b⁺ Ly6C^{int} Ly6G⁺ in mice and CD11b⁺ CD15⁺ CD33⁺ HLA-DR⁻ in humans. Both MDSC subsets suppress T cell-mediated adaptive immune responses; PMN-MDSCs preferentially produce peroxynitrite and prostaglandin E2 (PGE2), while M-MDSCs produce higher levels of nitric oxide (NO) through the action of inducible NO synthase (iNOS) and cytokines such as transforming growth factor β (TGF- β) to impair T cell responses.^{2,5,6} While arginase-1 (Arg1) is not absolutely required for the suppressive activity of MDSCs, proinflammatory cytokines (e.g., GM-CSF, interleukin-6 [IL-6], IL-4, and IL-10) may induce higher expression of Arg1, which enhances the immunosuppressive function of MDSCs.^{7,8} At the transcriptional level, the expression of iNOS is induced by transcription factors nuclear factor κ B (NF- κ B and STAT1 or the epigenetic modulator SETDB1 and may be inhibited by STAT3.^{5,9}

The development of tumor-associated MDSCs is regulated by multifaceted molecular pathways. Proinflammatory factors (e.g., GM-CSF, IL-6, M-CSF, G-CSF, PGE2, interferon γ [IFN- γ], etc.) and the hypoxic tumor microenvironment (TME) elicit pathological stress responses in myeloid progenitors that drive MDSC differentiation.^{2,3} MDSC differentiation is also augmented by unfolded protein responses (UPR) and elevated lipid metabolism, which both affect mitochondrial homeostasis.¹⁰⁻¹³ On the other hand, our knowledge of the regulatory circuits that sustain the metabolic adaptation and homeostasis of MDSCs is still incomplete. It remains a priority to identify multipotent therapeutic targets that control MDSC development.

V domain immunoglobulin suppressor of T cell activation (VISTA) (gene *Vsiv*, also known as GI 24, Dies-1, PD-1H, and DD1 α) is an inhibitory B7 family immune checkpoint protein.^{14,15} Studies from our group and others have shown that VISTA regulates peripheral tolerance and impairs anti-tumor immunity.^{14,16,17} Similar to PD-1, VISTA plays a broad role in regulating both myeloid cell-mediated and T cell-mediated anti-tumor responses.¹⁴⁻²³ VISTA on dendritic cells (DCs) and macrophages downregulates their responses following Toll-like receptor stimulation and reduces the production of T cell-stimulatory cytokines such as IL-12 and IL-27.^{15,24} In both melanoma and colon cancer models, antibody-mediated VISTA blockade elevates the expression of major histocompatibility complex (MHC) class II and genes involved in antigen presentation (IL-12, CD80, etc.) on tumor-infiltrating CD11b⁺ CD11c⁺ monocyte-derived DCs.^{22,24} Recent studies have demonstrated that VISTA is expressed in tumor-associated MDSCs, and blocking VISTA by global gene deletion or using antibodies partially ablates the suppressive effects of M-MDSCs.^{24,25,26} However, the suppressive action of VISTA in MDSCs is largely attributed to engaging a coinhibitory receptor, PSGL-1, in T cells.¹⁹ Extending beyond those findings, this study unveiled a mechanism by which VISTA promotes STAT3 activation and STAT3-dependent metabolic regulations that drive the differentiation of MDSCs.

RESULTS

Genetic deletion of VISTA impaired the differentiation of BM-derived M-MDSCs under normoxia and hypoxia conditions

While previous studies have indicated that VISTA is not required for normal myelopoiesis at a steady state,^{15,24,27} it is unclear how VISTA regulates the development of tumor-associated MDSCs. Because VISTA is not directly involved in the suppressive function of PMN-MDSCs, we focused on addressing the role of VISTA in regulating the differentiation of M-MDSCs.²⁴ We generated BM-derived MDSCs by stimulating immature myeloid progenitors with GM-CSF and IL-6, which are inflammatory cytokines often enriched in the TME and known to drive MDSC accumulation.²⁸⁻³¹ Wild-type (WT) and *Vsir*^{-/-} M-MDSCs were purified after a 4-day culture and examined for their suppressive activity. Consistent with the effects of VISTA-specific blocking antibodies, genetic deletion of VISTA in M-MDSCs diminished their ability to suppress T cell expansion (Figure 1A).

Aside from GM-CSF and IL-6, hypoxia is a critical TME factor that promotes MDSC differentiation by elevating STAT3 activation.³² VISTA expression on MDSCs was augmented by hypoxia (Figures S1A and S1B),²⁶ but it remains unknown how VISTA regulates MDSC differentiation under hypoxia. To address this, we exposed WT and *Vsir*^{-/-} BM M-MDSCs to hypoxia for 24 h before testing their suppressive function. Hypoxia enhanced the suppressive activity of both WT and *Vsir*^{-/-} M-MDSCs, and this effect persisted after reoxygenation (Figures 1B and 1C). *Vsir*^{-/-} M-MDSCs remained less suppressive than MDSCs under certain abundance (i.e., 1:16 and 1:32 under persistent hypoxia or 1:4 and 1:8 under transient hypoxia). These results indicate that VISTA promotes the suppressive function of M-MDSCs under normoxia and certain hypoxia conditions. It is noted that, under persistent hypoxia, the effects of MDSCs at higher abundance (1:4 and 1:8 ratios) were not relieved by VISTA deficiency, presumably due to saturating levels of T cell-inhibitory molecules (Figure 1B).

Next, we sought to determine the molecular defects of VISTA-deficient M-MDSCs. Arg1 and iNOS contribute to the suppressive function of MDSCs.³³ In BM-derived M-MDSCs, VISTA deficiency reduced the expression of Arg1 and iNOS under both normoxic and hypoxic conditions, as detected by flow cytometry and by western blotting (Figures 1D and 1E; Figure S1C). To understand the molecular basis that is associated with reduced Arg1 and iNOS expression, we analyzed the signaling events downstream of GM-CSF and IL-6. VISTA expression was detected in BM monocytic precursors such as clonogenic common monocyte progenitor (cMOPs) and monocytes (Figures S3A and S3B), and the expression of Gp130 (IL-6 receptor beta subunit) and CD131 (GM-CSF receptor beta subunit) was unaltered in *Vsir*^{-/-} cells (Figure S3C). Consistent with defective signaling, *Vsir*^{-/-} M-MDSCs showed impaired STAT3 phosphorylation at Y705 and S727 in response to IL-6 (Figure 1F). The acute activation of STAT3 in freshly isolated *Vsir*^{-/-} BM progenitor cells was also dampened (Figure S2). In addition to STAT3, we analyzed the signaling responses to GM-CSF and found that VISTA deletion inhibited ERK1/2 activation, which may have contributed to the phosphorylation of STAT3^{S727}, as indicated by previous studies (Figure 1G).³⁴⁻³⁶ In contrast to ERK1/2, STAT5 activation was not affected (Figure 1G).

Overexpressing the constitutively active STAT3 mutants (STAT3^{Y705E} and STAT3^{S727D})³⁷ rescued Arg1 expression in *Vsir*^{-/-} MDSCs (Figures 1H and 1I). Together, these results reveal the role of VISTA in promoting STAT3 and ERK1/2 activation, which may induce the expression of Arg1 and iNOS.³⁸⁻⁴¹

VISTA deficiency impairs polyamine biosynthesis and the mitochondrial metabolism in MDSCs

Arg1 hydrolyzes L-arginine into ornithine, which is catabolized by ornithine decarboxylase (ODC1), the rate-limiting enzyme during the biosynthesis of polyamines, including putrescine, spermidine, and spermine.^{42,43} ODC1 is reportedly a target of STAT3 either directly or indirectly.⁴⁴⁻⁴⁶ We found that ODC1 expression was greatly diminished in *Vsir*^{-/-} knockout (KO) MDSCs, particularly under hypoxic conditions (Figure 2A). Mass spectrometry analysis revealed significantly reduced intracellular putrescine levels in hypoxia-treated *Vsir*^{-/-} M-MDSCs (Figure 2B). A similar trend was seen under normoxia conditions. These results affirm the causal role of VISTA in promoting polyamine biosynthesis.

Polyamines are amino acid-derived polycations that interact with DNA, RNA, and proteins and regulate a wide range of biological processes, including gene expression, protein translation, and cell proliferation of many immune cell types.^{42,43} Previous studies have shown that depleting polyamine reduces MDSCs and affects macrophage polarization^{47,48} but the mechanism of action was not clear. We found that, in *Vsir*^{-/-} M-MDSCs, supplementing putrescine rescued both pSTAT3^{Y705} and pSTAT3^{S727} levels (Figure 2C). Conversely, inhibiting polyamine biosynthesis with an ODC1 inhibitor, difluoromethylornithine (DFMO), diminished STAT3 activation in WT M-MDSCs (Figure 2D). To understand how polyamines promote STAT3 activation, we investigated the potential involvement of casein kinase 2 (CK2), which has been implicated in the differentiation of PMN-MDSCs.^{49,50} We postulate that polyamines may stimulate CK2, which has been shown to promote JAK/STAT3 activation.^{51,52} We found that blocking CK2 inhibited Arg1 expression and that this effect was partially reversed by putrescine supplementation (Figure 2E). Thus, polyamines exert a positive feedback loop to sustain their own biosynthesis by promoting CK2 activity, STAT3 activation, and Arg1 expression. To affirm the mechanistic connection between STAT3 and polyamines, we examined the effects of a STAT3 inhibitor (Stattic) and putrescine supplementation on Arg1 expression in MDSCs. In both WT and *Vsir*^{-/-} MDSCs, Arg1 expression was diminished by Stattic treatment and rescued by putrescine supplementation (Figure 2F). Taken together, these results indicate the mutual dependence of STAT3 activation and polyamine biosynthesis and reveal that both are downstream “effector”, mechanisms of VISTA in driving MDSC differentiation.

Mitochondrial functions are regulated by activated STAT3 and polyamines.^{36,37,53,54} We hypothesize that, by promoting STAT3 activation and polyamine production, VISTA may augment mitochondrial respiration in MDSCs. In both normoxic (Figure 2G) and hypoxic (Figure 2H) MDSCs, VISTA deletion resulted in a significantly lower basal oxygen consumption rate (OCR), which is indicative of reduced oxidative phosphorylation

(OXPHOS); a lower extracellular acidification rate (ECAR), which is attributed to aerobic glycolysis and mitochondrial respiration; and a lower spare respiration capacity (SRC) (Figure 2I). Lower OCR and ECAR profiles revealed a quiescent bioenergetic state in *Vsir*^{-/-} MDSCs (Figure 2J). Supplementation of putrescine improved mitochondrial respiration in *Vsir*^{-/-} MDSCs (Figures 2K and 2L) and validated the causal relationship between polyamine and mitochondrial functions. To corroborate the impaired mitochondrial respiration, we examined intermediate metabolites from glycolysis and the tricarboxylic acid (TCA) cycle (Figures S4A and S4B). Although most metabolites were not significantly altered, the levels of reduced nicotinamide adenine dinucleotide (NADH) were lower in *Vsir*^{-/-} MDSCs, and conversely, the ratio of NAD⁺/NADH was higher than in WT cells, particularly under hypoxia conditions (Figure S4C). This result indicates an imbalanced redox state that is consistent with mitochondrial dysfunction.

To understand the molecular basis of mitochondrial dysfunction, we examined the hypusination of eukaryotic initiation factor 5A (eIF5a), which requires spermidine and is involved in mitochondrial biogenesis.^{53,54} However, *Vsir*^{-/-} MDSCs contained normal levels of hypusinated eIF5a (Figure S5A). Next, we assessed the expression of electron transport chain (ETC) complexes. The expression of ETC complexes I, III, and V was notably diminished in *Vsir*^{-/-} MDSCs (Figure 2M; Figure S5B). Putrescine supplementation partially rescued the expression of complex V (ATP synthase) in *Vsir*^{-/-} MDSCs. It is unclear why other ETC complexes were less responsive to putrescine treatment (Figure S5B), and we speculate that it may be partly due to oxidative damage resulting from excessive polyamine catabolism.^{55,56} Nevertheless, the rescue of ATP synthase expression was sufficient for the recovery of respiration. Putrescine also partially rescued Arg1 expression, presumably due to its effects on increasing STAT3 activation (Figure 2N). Altogether, these results support the notion that the VISTA/STAT3/polyamine axis plays a key role in promoting mitochondrial respiration in MDSCs.

VISTA deficiency alters gene expression and molecular pathways in BM-derived MDSCs

To gain insights into additional molecular pathways regulated by VISTA, we examined the transcriptome of WT and *Vsir*^{-/-} BM MDSCs by RNA sequencing (RNA-seq). Gene set enrichment analysis (GSEA) revealed overlapping sets of differentially expressed genes (DEGs) and molecular pathways in *Vsir*^{-/-} MDSCs under normoxia (Figures 3A-3D) and hypoxia (Figures 3E-3H). Pathways such as OXPHOS, Myc targets, MTORC1 signaling, E2F targets, and the UPR were significantly downregulated (Figures 3B, 3C, 3F, and 3G), whereas the IFN α / γ response pathways were upregulated in *Vsir*^{-/-} MDSCs. Under normoxic conditions, *Vsir*^{-/-} MDSCs upregulated genes that are involved in antigen presentation (e.g., *MHCII*, *Ciita*, *CD74*, etc.) and inflammatory signaling (e.g., *Ifi202b*, *Grap*, the *C1q* family, the Fc receptor family, Mmp-family genes, etc.), but downregulated genes controlling arginine metabolism (*Arg1*, *Nos2*, *Odc1*, *Ass1*, *Slc7a2*, and *Aldh18a1*), glycolysis (*Slc2a1*), lipid metabolism (*Pparg*), serine synthesis (*Phgdh*), and mitochondrial respiration (*Ndufa12*, *Ndufa9*, *Atp5g2*, *Idh2*, etc.) (Figure 3D). A similar cohort of genes was altered in hypoxic *Vsir*^{-/-} MDSCs (Figure 3H). Together, these gene signatures revealed the role of VISTA in MDSC differentiation through controlling cellular bioenergetics, proliferation, and responses to inflammation and stress. It is noted that VISTA deficiency did

not significantly alter the gene expression of the transcription factors *IRF8*, *C-Rel*, *C/EBPβ*, and *CHOP*, which are known regulators of MDSCs.^{2,3}

The upregulation of genes involved in antigen presentation and IFN α/β response pathways in *Vsir*^{-/-} MDSCs prompted us to determine whether VISTA regulates the differentiation of monocyte-derived DCs (moDCs) and whether this process is dependent on polyamines. When cultured with GM-CSF/IL-6/hypoxia, *Vsir*^{-/-} BM progenitors preferably expanded CD11c⁺MHC class II⁺ moDCs while restricting the accumulation of M-MDSCs (Ly6c^{hi} CD11c⁻Ly6g⁻) and PMN-MDSCs (Ly6c^{int} CD11c⁻ Ly6g⁺) (Figure 4A). Few F4/80⁺ macrophages were detected and were not enumerated. Putrescine supplementation suppressed the differentiation of moDCs but expanded M-MDSCs and PMN-MDSCs (Figure 4B). In contrast, polyamine depletion by DFMO treatment significantly expanded moDCs while reciprocally restricting the accumulation of M-MDSCs and PMN-MDSCs. The effects of DFMO were partially reversed by exogenous putrescine treatment (Figure 4B). Altogether, these results validated the causal role of polyamine in promoting MDSC expansion while restricting the differentiation of moDCs.

Next, we sought to validate the role of VISTA in regulating the differentiation of tumor-associated MDSCs. Because global VISTA KO mice tend to accumulate inflammatory cytokines that may inadvertently affect MDSCs,¹⁷ we generated mixed BM chimera mice to accommodate WT and *Vsir*^{-/-} myeloid cells in the same environment and examined tumor-infiltrating myeloid cells in the MC38 colon cancer model. We detected a diminished abundance of Ly6C^{hi} M-MDSCs and Ly6G⁺ PMN-MDSCs and a concomitant expansion of moDCs among *Vsir*^{-/-} myeloid cells (Figure 4C). Similar to BM-derived MDSCs, *Vsir*^{-/-} tumor-associated MDSCs downregulated genes involved in arginine metabolism (*Arg1*, *nos2*, and *Odc1*) (Figure 4D). Reduced expression of Arg1 and iNOS in *Vsir*^{-/-} M-MDSCs was further validated by flow cytometry (Figure 4E).

Transcriptomic analyses showed that VISTA deficiency extensively reprogrammed tumor-associated M-MDSCs (Figure 4F). *Vsir*^{-/-} tumor MDSCs downregulated molecular pathways that govern cellular energy production (glycolysis and hypoxia response), stress response (UPR), and proliferation (MTORC1 signaling and Myc targets) and enhanced responses to IFN α/γ (Figure 4G). A dysfunctional mitochondrial phenotype in *Vsir*^{-/-} M-MDSCs was substantiated by significantly lower mitochondrial membrane potential, while the total mitochondrial mass was not significantly altered (Figure 4H). These results strengthen the hypothesis that VISTA promotes the differentiation of tumor-associated MDSCs by establishing a transcriptomic program that augments cellular metabolism, proliferation, and immunosuppressive function.

Tumor-associated myeloid cells are composed of highly heterogeneous subsets. To determine whether VISTA regulates the heterogeneity of tumor-associated myeloid cells, we sorted WT vs. *Vsir*^{-/-} CD11b⁺ myeloid cells from tumor tissues and performed single-cell transcriptomic profiling with integrated cell surface protein expression through cellular indexing of transcriptomes and epitopes by sequencing (CITE-seq). After quality control and filtering, we obtained 12,675 WT and 8,601 *Vsir*^{-/-} myeloid cells. Unsupervised clustering gave rise to 11 clusters that were visualized by Uniform Manifold Approximation

and Projection (UMAP) (Figure 5A; Figure S6A). “Macrophages” were identified with high expression of *F4/80*, *Sirpa*, and *Mrc1*. Three clusters of CD11c⁺MHC class II⁺ DCs were identified: “inflammatory myeloid DCs”; “cDC1 DCs” expressing *CD103*, *Batf3*, and *XCR1*; and CCR7-expressing DCs. “PMN-MDSCs” were distinguished based on the high expression of *Ly6g*, *S100A8*, *S100A9*, and *Ptgs2*. The remaining monocytic MDSC populations were found to contain five heterogeneous clusters: “Monocyte” expressed high levels of *Ly6c* and *CCR2* and lacked other lineage markers (i.e., *CD11c*, *F4/80*, and *Ly6g*) and suppressive genes (i.e., *Arg1* and *iNOS*); “Activated_monocyte” was similar to “Monocyte” but upregulated *CD40*, *Csf2rb* (CD131), and *Tap1* expression; “Monocyte_Nos2” cells were similar to “Activated_monocyte” but further upregulated *Nos2* expression; “M-MDSC” was distinguished from other monocytic subsets based on higher expression of *Ccl2*, *Arg1*, and *iNOS*; “intermediate M-MDSC” was phenotypically similar to “M-MDSC” but expressed lower amounts of *Ccl2*, *Arg1*, and *iNOS* and higher levels of *CD84* and *Sirpa*. Protein expression of CD11c, Ly6G, and Ly6C was largely aligned with cluster identities of DCs, PMN-MDSCs, and monocytic subsets, respectively (Figures S6B and S6C). Analysis of cluster abundance revealed that VISTA deficiency drastically reduced percentages of PMN-MDSCs and reciprocally expanded moDCs (Figure 5B), which is consistent with flow-based analyses (Figure 4). Although the abundance of M-MDSCs appeared unchanged, we noted that multiple *Vsir*^{-/-} monocytic subsets, including “Monocyte,” “Activated_monocyte,” “Monocyte_Nos2,” “Intermediate_MDSC,” and “MDSC” subsets, expressed more CD11c protein than WT cells (Figure S6D), indicating that they are at intermediate stages of DC differentiation. The relative abundance of macrophages remained unaltered. Thus, these results suggest that VISTA deficiency promotes the differentiation of moDCs from monocytic precursors.

To understand the transcriptomic alterations in VISTA-deficient tumor MDSCs, we performed GSEA for each monocytic subset. We observed downregulated OXPHOS and upregulated inflammatory responses in *Vsir*^{-/-} monocytic cell clusters and M-MDSCs, which corroborated the gene signature in bulk Ly6C^{hi} M-MDSCs (Figure 5C; Figure S7A). A set of “enriched common genes” was identified in *Vsir*^{-/-} cells across all myeloid subsets (Figure S7B). Many “commonly upregulated” genes (i.e., *ApoE*, *C1q*-family genes, *CD74*, *Fcgr*-family genes, and *MHCII*-family genes) are involved in proinflammatory responses and antigen presentation, while “commonly downregulated genes” (i.e., *Chil1/3*, *IFI*-family genes, *ISG15*, etc.) are involved in cell proliferation. These results therefore solidify the role of VISTA in promoting the expansion and function of tumor MDSCs while conversely suppressing moDC differentiation.

Targeting MDSCs is a viable strategy to improve anti-tumor immunity.^{2,57} We hypothesize that targeting VISTA in monocytic cells will reduce MDSC accumulation and boost anti-tumor immunity. The CX3CR1 chemokine receptor is highly expressed in mononuclear phagocytes but not in granulocytes.^{58,59} To delete VISTA in monocytic lineages, we crossed VISTA floxed mice to *Cx3cr1*^{Cre/+} mice (*Vsir*^{fl/fl} *Cx3cr1*^{Cre/+}) and evaluated antitumor immune responses in the MC38 colon cancer model. Unexpectedly, MC38 tumors grew similarly in *Vsir*^{fl/fl} *Cx3cr1*^{Cre/+} mice and *Cx3cr1*^{Cre/+} WT littermates (Figure S8A). Flow analysis revealed inadequate VISTA deletion in tumor-associated M-MDSCs, PMN-

MDSCs, and moDCs (Figure S8B), presumably due to either low Cx3cr1 promoter activity or insufficient recruitment of VISTA-deficient monocytes into tumor tissues.

To boost the expansion and differentiation of Cx3cr1-expressing monocytes and their migration to tumor tissues, we resorted to inducing systemic inflammation by using Toll-like receptor agonists.⁶⁰ Because Toll-like receptor (TLR) stimulation promotes the expansion of MDSCs,^{33,60,61} we postulate that VISTA may play a more prominent role in promoting vaccine-induced myeloid expansion and immunosuppression. We treated MC38 tumor-bearing mice with a peptide vaccine containing TLR7/8/9 agonists and tumor antigen-specific peptides.^{62,63} While tumor growth was largely undeterred in WT mice, a portion of *Visr^{fl/fl} Cx3cr1^{Cre/+}* mice (6 of 8) rejected tumors and reached long-term tumor-free survival (Figure 6A). Tumor-free survivors were protected from tumor rechallenge, indicating the development of an effective memory response (Figure 6B). Next, we characterized tumor-associated myeloid cells in mice receiving reduced vaccine doses that permitted tumor growth. VISTA expression was diminished in tumor-associated M-MDSCs and PMN-MDSCs as well as in BM cMOPs, monocytes, and monocyte-like precursors of granulocytes (MLPG), the precursor of PMN-MDSCs⁶⁴ (Figures S9A and S9B). VISTA deletion was associated with reduced accumulation of M-MDSCs and a reciprocal increase of CD11C⁺MHC class II⁺ DCs (Figure 6C) as well as diminished expression of Arg1 and iNOS in M-MDSCs (Figures 6D and 6E). CD8⁺ cytotoxic T cells from VISTA KO tumors demonstrated better effector functions by expressing more effector cytokines (IFN- γ and TNF- α) and granzyme B (Figure 6F). Last, we corroborated these results in the B16F10 melanoma model. Myeloid-specific VISTA deletion significantly inhibited melanoma growth following treatment with a peptide vaccine (Figure S10A). Tumor reduction was associated with reduced M-MDSCs, accumulation of myeloid DCs, and downregulated Arg1 expression (Figures S10B and S10C). Altogether, these results suggest that ablating VISTA in myeloid progenitors effectively reduces MDSC accumulation and boosts T cell-mediated tumor control.

VISTA expression in human tumor-associated myeloid cells has not been well studied. We first examined public datasets via the cBioPortal For Cancer Genomics.^{65,66} A significant correlation of expression was seen between VISTA and ARG1 in several cancer types, including pancreatic ductal adenocarcinoma, endometrial carcinoma, lung adenocarcinoma, and metastatic melanoma (Figure 7A). Next, we examined VISTA gene expression in a public single-cell RNA-seq dataset from melanoma patients treated with immune checkpoint inhibitors (ICIs).⁶⁷ Tumor-associated myeloid cells were identified based on the author's original cell type determinations, including "Dendritic_Cells" and "Monocytes/Macrophages," which were validated by the expression of myeloid cell marker genes (Figure S11A). Gene expression of ARG1/2 was very low across all myeloid subsets, presumably due to insufficient sequencing depth, and prevented accurate quantitation. VISTA gene expression (*c10orf54* and *Visr*) was abundant in monocyte/macrophage populations. Using CD84 as a surrogate marker to identify MDSCs,^{2,68} we found that the abundance of VISTA⁺CD84⁺ MDSCs, shown as percentages among total TILs, was significantly associated with resistance to ICI therapy in both pre-ICI and post-ICI tissues (Figure S11A). In pre-ICI tissues, the abundance of total VISTA⁺TILs, but not CD84⁺

cells, was associated with non-response, whereas in post-ICI tissues, the abundance of total CD84⁺ TILs, but not VISTA⁺ TILs, was prognostic (Figures S10C and S10D).

Last, we sought to validate the prognostic role of myeloid-expressed VISTA and ARG1 in endometrial cancer because this cancer type showed correlated expression of VISTA and ARG1 based on cBioportal analysis (Figure 7A). We first examined M-MDSCs (CD11B⁺CD33⁺HLA-DR^{lo}CD14⁺) and PMN-MDSCs (CD11B⁺CD33⁺HLA-DR⁻CD15⁺) in surgically removed human endometrial tumor tissues (Figure 7B; Figure S12). Tumor-associated PMN-MDSCs and M-MDSCs expressed both VISTA and ARG1. Next, we performed multiplexed immunofluorescence (IF) imaging analysis in an endometrial tumor tissue microarray (TMA) that included archival tumor specimens from 121 patients, with assessable TMA cores from 93 patients following quality control (Table S1). Multiplexed panels were applied to detect VISTA and ARG1 expression on tumor-associated myeloid antigen-presenting cells (APCs, CD11B⁺HLA-DR⁺) or MDSCs (CD11B⁺HLA-DR^{lo}) (Figure 7C). Due to technical limitations of multiplexed IF, we were not able to reliably distinguish PMN-MDSCs vs. M-MDSCs. Because a significant portion of tumor-associated PMN-MDSCs may originate from monocytic progenitors with phenotypic resemblance of M-MDSCs,^{32,64,69,70} we postulate that VISTA and ARG1 on total MDSC populations may be more relevant to prognosis. Supporting this, higher percentages of VISTA⁺ARG1⁺CD11b⁺HLA-DR^{neg} MDSCs (Figure 7D) or VISTA⁺ARG1⁺CD11B⁺ myeloid cells (inclusive of both HLA-DR⁺ APCs and negative MDSCs) (Figure 7E) among the total CD11B⁺ myeloid cells were associated with worse disease-free survival (DFS) and overall survival (OS). VISTA or ARG1 expression alone was not prognostic for DFS, although it was notable that VISTA expression alone was prognostic for OS (Figure S13). CD11B⁺HLA-DR⁺ APCs were of very low abundance in most samples and were not reliably enumerated. VISTA expression was not detected on tumor cells (PanCK⁺). No prognostic associations were found for the overall abundance of various tumor-infiltrating CD4⁺ and CD8⁺ T cells, Foxp3⁺CD4⁺ regulatory T cells (Tregs), PD1⁺ T cells, PD-L1⁺ T cells, or ratio of Tregs/CD8⁺ T cells (Table S1). Together, these data substantiate the role of VISTA as a promoter of MDSC-mediated immunosuppression in human cancers.

DISCUSSION

M-MDSCs and PMN-MDSCs are the major roadblocks that prevent successful anti-tumor immunity.¹⁻⁴ Although it is known that a chronic inflammatory milieu and a hypoxic environment induce aberrant MDSC differentiation, the regulatory circuits governing MDSC differentiation programs remain incompletely understood, and new approaches to targeting MDSC differentiation remain a topic of intense research. In this context, this study has shown that VISTA, a next-generation immune checkpoint protein, is a critical regulator of mitochondrial bioenergetics, differentiation, and function of M-MDSCs.

Although it has been reported that VISTA contributes to the suppressive function of MDSCs,^{24,26} the mechanism was attributed to the ability of VISTA to control myeloid cell-derived cytokines such as IL-12 or to engage a T cell coinhibitory receptor, PSGL-1. This study describes a distinct mechanism whereby VISTA functions to steer myeloid differentiation; VISTA promotes STAT3 activation, which establishes a transcriptomic and

metabolic program that drives the differentiation of MDSCs. VISTA deficiency impaired STAT3 activation, reduced Arg1 expression, and inhibited polyamine biosynthesis. These multitudinous effects causally reduced the expression of ETC complexes and caused mitochondrial dysfunction. In addition, VISTA/STAT3 deficiency reprogrammed the global transcriptomic program that supports the differentiation and expansion of MDSCs.

How do polyamines contribute to mitochondrial functions and MDSC differentiation? Although polyamines such as spermidine could promote mitochondrial function by promoting the hypusination of eIF5a,⁵³ we show that *Vsir*^{-/-} MDSCs contained normal levels of hypusinated eIF5a. Alternatively, we postulate that polyamines may indirectly regulate mitochondrial function by promoting CK2 activity and sustaining STAT3 activation because putrescine supplementation enhanced STAT3 activation, while DFMO treatment reduced STAT3 activation. STAT3 is known to regulate cellular metabolism by inducing metabolic gene expression as well as directly interacting with mitochondrial ETC complexes and promoting OXPHOS.^{37,71-73} In addition to STAT3-dependent effects, polyamines may also regulate mitochondrial bioenergetics by directly augmenting fatty acid oxidation.⁷⁴

In addition to mitochondrial dysfunction, our studies have revealed an extensive reprogramming of gene expression in VISTA-deficient MDSCs. Multiple molecular pathways (i.e., the OXPHOS, Myc targets, MTORC1 signaling, E2F targets, and UPR pathways) were downregulated, which negatively affected cellular metabolism, stress responses, and expansion. The transcriptomic changes in *Vsir*^{-/-} MDSCs may be the result of not only STAT3-dependent activities but also polyamines that may directly interact with DNA, transcription factors, and chromatin-remodeling proteins.^{43,54,75} These secondary and tertiary effects solidify the differentiation trajectory of MDSCs.

Tumor-associated M-MDSCs maintain the potential to differentiate into DCs and macrophages under permissive conditions.⁷⁶ In both *ex vivo* BM cultures and tumor-bearing mice, we found that VISTA deficiency led to an expansion of moDCs and a concurrent reduction of MDSCs. The abundance of macrophages was not affected by VISTA. Pathway analysis revealed that VISTA deficiency enhanced cellular responses to IFN α / γ and upregulated genes involved in antigen presentation, such as Ciita, CD74, and MHC class II genes, which promote the differentiation and maturation of moDCs.⁷⁷ This effect may be due to the reduced STAT3 signaling because STAT3 is known to inhibit DC differentiation and function.⁷⁸⁻⁸¹ In addition, we have unveiled that polyamines act as the key downstream effector of VISTA and causally steer myeloid differentiation; blocking polyamine production in WT monocytic progenitors curbed MDSC differentiation and induced moDC expansion, while supplementing putrescine in *Vsir*^{-/-} progenitor cells led to opposite effects.

Understanding and targeting metabolic regulators of MDSCs may improve cancer treatment.^{2,82} Multiple approaches have been suggested to target metabolic regulators in MDSCs. For example, inhibiting STAT3, reducing glucose uptake, inhibiting c-Rel/mTOR/HIF1 α -dependent glycolysis, blocking CD36 and FATP2-dependent lipid uptake, or inhibiting fatty acid oxidation by blocking β -adrenergic receptors has shown anti-tumor effects.^{2,11-13,82-84} Our study adds VISTA as a promising target for inhibiting the differentiation of tumor-associated MDSCs. It is noted that chemical inhibitors have the

drawbacks of limited bioavailability and high systemic toxicity, making it challenging to achieve specific and effective blockade of MDSCs. The notable advantages of VISTA as a therapeutic target include its targetability as a cell surface protein and restricted expression within immune cells and on tumor-associated myeloid cells, thereby minimizing off-target effects.^{15,22,24} VISTA acts as an “upstream enabler” that amplifies the responses of monocytic progenitors to TME factors, which is arguably a more advantageous target than downstream factors. Supporting this, we have shown the proof of principle that blocking VISTA effectively diminished the STAT3/polyamine cycle and caused multitudinous defects in MDSC bioenergetics, accumulation, and suppressive function. The prognostic significance of VISTA/ARG1 expression in human cancers lends further support to the notion that blocking the VISTA/STAT3/polyamine axis will reduce MDSC-mediated immunosuppression and benefit anti-tumor immunity.

Limitations of the study

While this study has demonstrated a causal role of VISTA in promoting STAT3 activation, polyamine biosynthesis, mitochondrial respiration, and MDSC differentiation, we did not identify the molecular intermediates that link VISTA to STAT3. The expression of IL-6 and GM-CSF receptors was not affected by VISTA, nor did we detect any physical interactions of VISTA with these receptors. Although we have shown that, in MDSCs, polyamines causally promote mitochondrial respiration and that this process is independent of EIF5a hypusination, we did not identify any direct mode of action by which putrescine regulates mitochondrial respiration. Alternatively, our results may assign an indirect role of putrescine in promoting mitochondrial function by sustaining STAT3 activation. Last, while we show that VISTA expression in human tumor-associated MDSCs is associated with poor survival, we did not show whether therapeutically blocking VISTA may impair the metabolic fitness and expansion of human tumor-associated MDSCs.

STAR★METHODS

RESOURCE AVAILABILITY

Lead contact—Further information and requests for resources and reagents should be directed to and will be fulfilled by the lead contact, Li Lily Wang, wangl9@ccf.org.

Materials availability—Further information and requests for resources and reagents generated in this report should be directed to and will be fulfilled by the lead contact, Li Lily Wang, wangl9@ccf.org.

Data and code availability

1. Single-cell RNA sequencing data and bulk RNA sequencing data of BM-derived and tumor-associated MDSCs have been deposited on the National Center for Biotechnology Information Gene Expression Omnibus (GEO) under the accession number GSE244545 and GSE244797 and are publicly available.
2. Code for data analysis is available upon reasonable request to the corresponding author.

3. Any additional information required to reanalyze the data reported in this paper is available from the lead contact upon request.

EXPERIMENTAL MODEL AND STUDY PARTICIPANT DETAILS

Study approval—All animal protocols were approved by the Institutional Animal Care and Use Committee of Lerner Research Institute at Cleveland Clinic Foundation. All methods were performed following the relevant guidelines and regulations. Studies of human endometrial cancer tissues were approved by the Institutional Review Board of University Hospitals Cleveland and Case Western Reserve University School of Medicine.

Human samples—For multiplexed immunofluorescence studies, we utilized an endometrial cancer tissue microarray (TMAs) that contained archival tumor tissues from 121 women diagnosed with endometrial cancer at University Hospitals Cleveland Medical Center, Cleveland, Ohio, between 2006 and 2012. This included 58 self-reported Black/African American women, as well as 63 self-reported American women, matched for age, tumor stage, and histologic subtype. Within the cohort, 79 cases (65%) were of the endometrioid histologic subtype and 42 cases (35%) were of the non-endometrioid subtype, including 29 serous, 8 clear cell, and 5 mixed endometrial carcinomas. Eighty-eight (73%) patients had early-stage disease (FIGO stages I or II) and 33 (27%) had advanced stages (FIGO III or IV). About two-thirds of the patients ($n = 73$, 60%) were obese with a BMI of 30 or greater, while 26 (22%) were non-obese (BMI <30) and data on BMI was missing for 22 (18%). The follow-up time for survival outcomes was from 2006 to 2018, with a median time to censoring of 75 months, and a median observation time (censored and uncensored) of 55 months. During the follow-up period, there were 25 disease recurrences and 45 deaths. Among those, the median time to recurrence was 18 months, and the median time to death was 29 months. Neither median disease-free survival nor median overall survival was reached during the follow-up period. Patient characteristics are summarized in Table S4.

For flow analysis of fresh tumor tissues, deidentified specimens of cancerous tissues were collected in sterile tubes containing RPMI media and immediately sent to the laboratory for processing. Tissues were digested with Liberase TL (Roche, Pleasanton, CA) and DNase (Sigma, St Louis) at 37°C for 20 min, dissociated into single-cell suspensions, stained by antibodies, and analyzed by flow cytometry.

Animals—C57BL/6N (H-2^b, CD45.1) and congenic C57BL/6N (H-2^b, CD45.2) mice were purchased from Charles River Laboratories. *Vsir*^{-/-} mice were originally generated on a C57BL/6N background and were obtained from Mutant Mouse Regional Resource Centers (www.mmrrc.org; stock no. 031656-UCD).^{17,23} To establish the colony, we crossed the original *Vsir*^{-/-} mice with C57BL/6N mice for one generation and inter-crossed heterozygous offsprings to obtain *Vsir*^{-/-} and WT littermates. *Vsir*^{fl/fl} mice were as previously described⁸⁵ and bred with *Cx3CRI*^{Cre} (Jax, stock no. 025524) to create myeloid-specific VISTA conditional KO mice (*Vsir*^{fl/fl} *Cx3CRI*^{Cre/+}) and WT littermates (*Cx3CRI*^{Cre/+}). Animals were maintained in a specific pathogen-free facility at Lerner Research Institute (LRI), Cleveland Clinic Foundation, Cleveland, OH. All preclinical experiments used sex and age-matched mutant mice and WT littermates without investigator

blinding. Both male and female mice were studied. All experiments were repeated at least two times. All data points and p values reflect biological replicates.

Cell lines—MC38 murine colon cancer cells (Kerafast, Boston, MA) and B16F10 melanoma cells (ATCC), were cultured in bicarbonate-free HEPES-free RPMI-1640 supplemented with 10mM HEPES (Life Technologies), 10% FBS, sodium pyruvate, 2 mM L-glutamine, and 50 μ M β -mercaptoethanol, and penicillin/streptomycin (Life Technologies). Cells were tested for mycoplasma contamination every 3–4 months, using MycoAlert Mycoplasma Detection Kit (Lonza Inc, Allendale, NJ). Cells were maintained at passages below 10 and detached using an accutase cell detachment medium (Sigma) for passage.

METHOD DETAILS

Real-time quantitative RT-PCR (qRT-PCR)—The total RNA was prepared using the RNeasy Kit (Qiagen, Hilden, Germany). cDNA was synthesized by using PrimeScript 1st strand cDNA Synthesis Kit (Takara, cat no. 6110B). DNA was amplified by using iTaq Universal SYBR Green Supermix (Bio-Rad, cat no. 1725121). Quantitative qRT-PCR was performed using Bio-Rad iQ5 Real-Time PCR System (Bio-Rad, Hercules, CA). Primer sequences are described in the following: Arg1 (forward: ggcaacctgtctccttctc; reverse: acacgatgtctttggcagat); inos (forward: cctctctgatcttgtgttga; reverse: caaccgagctcctggaac); Odc1 (forward: cgtcattggtgtgagcttc; reverse: gtatctgcctggctcagcta); 18s (forward: aaccctgtgaacccatt; reverse: ccatccaatcggtagtagcg).

BM cell culture, hypoxia and inhibitor treatment, and metabolite measurement

—To generate BM-derived MDSCs, WT or *Vsir*^{-/-} Ly6C⁺ monocytic progenitors were isolated from BM after lineage depletion using biotinylated Abs against CD4, CD8, CD3, B220, NK1.1, F4/80, CD11c, and Ly6g and applying EasySep Mouse Streptavidin RapidSpheres Isolation Kit (Stemcell Tech, Cat# 19860). Monocytic progenitors were cultured in RPMI media supplemented with GM-CSF (10 ng/mL), IL-6 (10 ng/mL), 10% FBS, 2 mM L-glutamine, and 50 μ M 2-mercaptoethanol for 4–5 days. When indicated, hypoxia treatment was performed by transferring cells to a 1% O₂ chamber during the last 24 h of culture. Cells were harvested using a cell scraper for downstream analyses. M-MDSCs were purified after depleting DCs, macrophages, and neutrophils/PMN-MDSCs, using a biotinylated antibody cocktail specific for CD11C, F4/80, and Ly6G and streptavidin-conjugated beads (EasySep Mouse Streptavidin RapidSpheres Isolation Kit, Stemcell Tech, Cat# 19860). The purity of M-MDSCs (CD11b⁺ Ly6C^{hi} Ly6G^{neg}) was verified using flow cytometry as > 90%. To examine the inhibitory function of MDSCs, purified M-MDSCs were co-cultured with OT1 whole splenocytes (50,000) at ratios of 1:4, 1:8, 1:16, and 1:32, in the presence of SIINFEKL peptide (100 pg/mL) in the U bottom 96 well plates. Triplicated wells were plated for each condition. After 72 h stimulation, cells in the plates were stained with the Live/Dead viability dye (ThermoFisher) together with an anti-CD8 antibody for 15 min. Cells were analyzed by a MACSquant flow cytometer, which enables accurate enumeration of expanded live OT1 cells.

For *ex vivo* treatment with inhibitors or chemicals, DFMO (400 μ M) (Tocris Bioscience, Fisher Scientific, Cat no. 27-611-0), or putrescine (800 μ M) (Fisher Scientific, Cat no. ICN10044105), or STAT3 inhibitor (2 μ M), or CK2 inhibitor (20 μ M), or combinations when indicated, were added to BM cell culture on day 2. Hypoxia treatment was performed by transferring cells to the 1% O₂ chamber during the last 24 h of the culture. Cells were harvested on day 4 or 5 as indicated for downstream analyses.

For immunoblot analysis, BM-derived MDSCs were re-stimulated with GM-CSF (50 ng/mL) or IL-6 (50 ng/mL) for the indicated time. Cells were lysed in RIPA buffer (50 mM Tris pH 7.4, 150 mM NaCl, 1.0% NP-40, 0.5% Deoxycholic Acid, 0.1% SDS, 1 mM EDTA, 1 mM EGTA, 5 mM sodium pyrophosphate, 50 mM NaF, 10 mM β -glycerophosphate) supplemented with protease and phosphatase inhibitors at indicated time points. Phosphorylated and total levels of signaling proteins or mitochondrial proteins were examined by Western Blotting. Protein levels were quantified using ImageJ.

For measuring intracellular polyamine levels, M-MDSCs were harvested as described above, washed with ice-cold PBS, and resuspended in ice-cold 80% methanol (methanol/water, 80/20, v/v). The cell/methanol mixture was frozen/thawed twice before centrifugation at 18,000 rcf for 15 min at 4C °. Cleared supernatants were dried overnight at 4C in a refrigerated SpeedVac concentrator and resuspended in water. Intracellular polar metabolites were analyzed by Liquid Chromatography with tandem mass spectrometry (LC-MS-MS) on an AB/SCIEX 5500 QTRAP system (BIDMC metabolomics core service).⁸⁶ Metabolic alterations were annotated using the MetaboAnalyst platform.⁸⁷ The ion counts of the respective metabolites were normalized to the total ion counts per sample and then compared between three biological replicates per sample.

To test STAT3 mutants: WT murine STAT3 plasmid was purchased from Origene Inc and used as the cloning template. STAT3^{Y705E} and STAT3^{S727D} mutants were generated via site-directed mutagenesis and cloned in frame with GFP at the C terminus. A mitochondrial localization sequence (MSVLTPLLLRGLTGSARRLPVPRAKIHSLPPEGK) derived from human Cox8a was cloned in frame with the N terminus of STAT3^{S727D}. The complete expression cassettes were cloned into a retroviral vector pBABE-puro (Addgene Inc). STAT3 plasmids were transfected into HEK293T cells along with packaging vectors using Lipofectamine transfection reagent (ThermoFisher). Retrovirus was harvested from the supernatant and used to transduce BM cells cultured in GM-CSF and IL-6. BM cells were harvested on day 4 and examined by flow cytometry.

Seahorse metabolic flux analysis—Assay components were from the Agilent Seahorse XF cell Mito stress test kit (cat no. 103015-100). The real-time OCR and ECAR were simultaneously recorded in an XF96 extracellular flux analyzer (Agilent Bioscience). WT and *Vsir*^{-/-} M-MDSCs were plated in media RPMI (Agilent, catalog no. 103576-100) supplemented with 2% FBS, 1% glucose, 1% pyruvate, and 1% glutamine, at 1.7×10^5 cells per well in an XF96 sensor cartridge plate. To facilitate cell adherence, the plate was pre-coated with 25ul of Poly-D-Lysine (ThermoFisher, cat no A3890401) at RT for 30 min and washed three times with PBS before the assay. Cells were kept in a non-CO₂ incubator at 37C° for 1 h before analysis. Three or more consecutive measurements were obtained

under basal conditions and after the sequential addition of 1 μ M oligomycin, 3.0 μ M fluoro-carbonyl cyanide phenylhydrazone (FCCP), 0.1 μ M rotenone plus 0.5 μ M antimycin A, and 10 mM 2-deoxy-glucose (2-DG) (all drugs were from Sigma). Basal oxygen consumption can be established by measurement of OCR in the absence of drugs. Maximal OCR was reached after the addition of FCCP as expected. SRC is calculated as the difference between basal OCR and maximal OCR.

Generation of BM chimera mice and tumor models—To generate BM chimera mice, BM cells from naive WT (CD45.2) and *Vsir*^{-/-} mice (CD45.1) were isolated, RBC lysed, and mixed at a 1:2 ratio, and transferred into lethally irradiated (1,200 rads) WT hosts (CD45.2). We chose a 1:2 ratio to allow sufficient numbers of *Vsir*^{-/-} MDSCs to develop in tumor-bearing mice for flow analyses. At 7–8 weeks post reconstitution, chimera mice were inoculated with MC38 tumor cells (1×10^6) on the flank. Tumors were harvested on days 12–14 (~8–9 mm in diameter). Tumor tissues were digested at 37°C for 20 min with Liberase TL (Roche, Pleasanton, CA) and DNase (Sigma, St Louis) to obtain single-cell suspensions. Myeloid cell subsets and mitochondria were stained with a viability dye and lineage markers. When indicated, cells were stained with MitoTracker Green FM and Deep Red FM (ThermoFisher Scientific, Waltham, MA) to measure mitochondrial mass and membrane potential. For detecting intracellular Arg1 and iNOS, cells were fixed and permeabilized with a Foxp3 staining buffer set (ThermoFisher Scientific, Waltham, MA), and stained with Arg1 and iNOS-specific antibodies. Cells were analyzed by flow cytometry using either an LSR II flow cytometer (BD Biosciences, San Jose, CA) or MACSquant16 analyzer (Miltenyi Biotec Inc, Charlestown, MA). Data were analyzed with FlowJo version 9.9.6 analysis software (Tree Star, San Carlos, CA).

To determine the effects of myeloid-specific VISTA deletion in anti-tumor immunity, myeloid-specific VISTA conditional KO mice (*Vsir*^{fl/fl} *Cx3CR1*^{Cre/+}) and WT littermates (*Cx3CR1*^{Cre/+}) were inoculated with MC38 colon cancer cells (100,000) or B16F10 melanoma cells (60,000) on day 0. On day 3, mice were treated subcutaneously on the flank with a peptide vaccine containing CpG (30 μ g), and R848 (50 μ g) as adjuvants and peptides derived from known tumor-associated antigens (50 μ g), including Adpgk (HLELASMTNMELMSSIVHQ) and Rpl18 (KAGGKILTFDRLALESPK) for the MC38 model, or TRP2 (SIYDFVWL) peptide for the B16F10 model.^{24,62,63} Tumor growth was monitored with a caliper every 3–4 days. To dissect the phenotypes of tumor-infiltrating immune cells, mice bearing tumors were treated with a 50% reduced vaccine dose containing peptides (25 μ g), CpG (15 μ g), and R848 (25 μ g). When tumors reached 8–10 mm in diameter (~ day 14–18 after vaccine treatment), depending upon the models), tumor tissues were harvested and examined by flow cytometry.

Transcriptomic analysis—For NGS RNA sequencing: WT and *Vsir*^{-/-} BM-derived M-MDSCs or tumor-associated M-MDSCs (Ly6C^{hi} Ly6G^{neg} CD11C^{neg}) were purified by flow sorting. Total RNA was isolated using Rneasy mini kits (Qiagen Sciences, Germantown, MD). cDNA library was prepared using SMART-Seq v4 ultra-low input cDNA Library Construction Kit (Takara Bio, San Jose, CA) or TruSeq Library kit (Illumina, San Diego, CA) and sequenced using NovaSeq NGS platform. Post-sequencing FASTQ files were

aligned to gene code release M25 (GRCm38.p6) with STAR aligner with default parameters version 2.7.6a. Aligned fragments were then counted and annotated using Rsamtools v1.8. Quality control was performed on BAM files using RSeQC to identify the quality of RNA alignment. Normalized reads were obtained using DESeq2. Batch correction was performed using Limma Voom, and batch-corrected counts were used for plotting abundance.

Differential gene expression analysis was conducted using the DESeq2 package and was performed using a generalized linear model with the Wald statistical test, with the assumption that underlying gene expression count data were distributed per a negative binomial distribution with DESeq2. GSEA analysis was performed based on the ranked list of differentially expressed genes (DEGs) by log fold change value using the R package GSVA. Plotting GSEA results was performed using the enrich plot R package. Hallmark gene sets were used for GSEA analysis downloaded from gsea-msigdb. Leading edge genes were plotted from pathways to the genes driving enrichment for biological interpretation. Heatmaps were generated using R package ComplexHeatmap Version 2.13.1.

For Single-Cell RNA-seq analyses: Single-cell transcriptomic profiling was performed with integrated cell surface protein expression through Cellular Indexing of Transcriptomes and Epitopes by Sequencing (CITE-seq). Tumor-associated myeloid cells were stained with a fluorescent anti-CD11b antibody together with TotalSeq B antibodies (Biolegend) that are compatible with V3.1 chemistry. These include Ly6C (Cat no. 128053), Ly6G (Cat no. 127659), and CD11c (Cat no. 117359). The concentration of each antibody was titrated to ensure specificity. Viable cells were blocked using an anti-CD16/32 FCR blocker (Cat no.101319) for 10 min before incubating with antibodies on ice for 20 min. CD11b⁺ myeloid cells were sorted using a BD FACSAria sorter (BD Biosciences, San Jose, CA).

Viable sorted cells were washed three times before being processed using 10X genomics Feature barcoding protocol and workflow with v3.1 3' technology. The single-cell RNAseq libraries are prepared by the Genomics Core facility at Lerner Research Institute. The single-cell RNAseq libraries are prepared according to the manufacturer's Chromium Single Cell 3' v3.1 with Feature Barcode technology for Cell Surface Protein (CSP) protocol. Briefly, cDNA for the 3' gene expression library was initially synthesized from polyadenylated mRNA, and DNA for the CSP library was synthesized from the cell surface protein feature Barcode. A minimum of 1 ng of cDNA was used to begin fragmentation, followed by end-repair, adapter ligation, and sample indexing. Each sequencing library including the CSP library was tagged with a dual index (10-nucleotide long each) sample barcode that identifies from which sample a sequence was derived. In addition, 12-base unique molecular indexes (UMIs) were introduced to reduce duplicate reads. Constructed libraries are pooled and quantified using a Quantabio Q cycler. NovaSeq 6000 RapidRun flow cells are used to sequence a minimum of 20,000 read pairs per cell for the Gene expression library and a minimum of 5,000 read pairs per cell for the Cell surface protein library using specifications recommended by the manufacturer (10X Genomics, document # CG000317).

Separate feature barcoding libraries were sequenced targeting 5,000 reads per cell at 10,000 cells per sample and were mapped to cells using Cell Ranger software. Antibody counts were compiled with gene expression data in Seurat V4.0 software and normalized via

CLR normalization methods for plotting. Raw data generated were aligned to mm10 with the mm10-2020 reference built and provided by 10X genomics. Sequencing depth and cell-ranger outputs were recorded and shown in Table S3. Post data alignment Seurat Version 4.0. in R version 4.1 was used for all downstream analysis and data integration. For each cell, the percentage of mitochondrial and ribosomal genes was calculated and used to filter out dead/dying cells. Cells were included for subsequent analysis if they contain at least 350 features of RNA and less than 30% mitochondrial content. Quality control parameters are shown in Table S3. After normalization, samples were integrated using the Harmony R package (<https://portals.broadinstitute.org/harmony/>). Clusters were subsequently generated using Seurat functions and were manually identified using top marker genes as well as using the FindAllMarkers function in Seurat with default parameters. To detect and visualize the differentially abundant (DA) subpopulations within WT vs. *Vs1r*^{-/-} myeloid cells, we applied an R package implementation of DA-seq algorithms (<https://github.com/KlugerLab/DAseq>).⁸⁸

Expression analysis in cBioPortal for Cancer Genomics—The cBioPortal for Cancer Genomics (<http://cbioportal.org>) is an open-access web resource for analyzing and visualizing cancer multi-omic data.^{65,66} In the present study, proteomic datasets from studies of pancreatic ductal adenocarcinoma, endometrial carcinoma, and lung adenocarcinoma, or transcriptomic datasets from studies of metastatic melanoma were queried for the expression levels of VISTA and ARG1.⁸⁹⁻⁹² The correlation of protein or gene expression was plotted according to the online instructions of the cBioPortal.

Single cell RNA-seq datamining—We sought to examine the expression of VISTA in tumor-associated myeloid cells in a public single-cell RNA-seq dataset from studies by Sade-Feldman et al.⁶⁷ This study describes TILs from immunotherapy-treated patients and contains clinical response annotations. We downloaded the dataset and used Seurat (v4.3.0) package in R for this analysis. Data were processed according to the filtering instructions in the original paper. We identified subsets of TILs based on authors' definitions of cell types, including Dendritic Cells, Monocytes/Macrophages, Cytotoxicity Lymphocytes, Exhausted CD8, Exhausted HS CD8 T cells, Lymphocytes, Lymphocytes Exhausted, Memory T cells, and Tregs. Cells were stratified based on treatment groups (i.e., pre-treatment vs. post-treatment) and clinical responses (responders vs. non-responders). We determined the percentages of cells expressing VISTA, CD84, or both among total TILs. We used the Wilcoxon signed-rank test (`Wilcox.test` function in R) to determine the statistical significance. For patients who had two post-treatment specimens collected that were assigned with the same response categories, we merged their post-treatment samples to calculate cell counts and percentages. We excluded samples from three patients who had two post-treatment samples collected but one was designated as “non-response” while another as “response”.

Multispectral imaging of endometrial cancer tissues and image analysis—TMA were constructed using 3–4 tumor cores (0.6 mm diameter) per case, covering areas in the center and periphery of tumor tissues. Consecutive TMA sections of 4- μ m thickness were used for H&E staining. Single-plex immunohistochemistry staining was performed

using clinically established routine IHC protocols on automated stainers and results were evaluated by manually quantifying the number of positive lymphocytes per TMA tumor core (averaged across all available TMA cores per patient) for CD8, CD4, FoxP3, PD1, and PD-L1.

Multi-plex immunofluorescence staining was performed using antibodies specific for pan-cytokeratin, CD11B, HLA-DR, VISTA, and ARG1. Staining was performed using the Discovery ULTRA automated stainer from Roche Diagnostics (Indianapolis, IN). In brief, antigen retrieval was performed using a Tris/borate/EDTA buffer (Discovery CC1, 06414575001; Roche), pH 8.0 to 8.5. Antigen denaturing was performed using a citrate buffer (Discovery CC2, 05424542001; Roche). Time, temperatures, and dilutions are listed below. The antibodies were visualized using the OmniMap anti-Rabbit HRP (05269679001; Roche), and OmniMap anti-Mouse HRP (05269652001; Roche) in conjunction with the Akoya Biosciences (Marlborough, MA) Opal Fluorophores, listed with their respective antibodies. The slides were counterstained with Spectral Dapi (FP1490; Akoya Biosciences).

Stained slides were imaged using the Vectra Polaris Automated Quantitative Pathology Imaging System (Akoya Bioscience) and the component images for each marker were obtained by unmixing the multi-spectral images in inForm (Akoya Bioscience, version 2.6). Component images resulting from the unmixing workflow were stitched to whole slide images and saved as OME-TIFF⁹³⁻⁹⁵ for analysis and archival using QuPath.⁹⁶

Whole slide images of stained TMA cores were analyzed using an open-source image analysis software QuPath version 0.4.2. Using the “TMA dearrayer” command in QuPath, TMA cores were identified followed by manual correction. TMA cores with little or no tissues were marked as “missing” and excluded from the analysis. TMA analysis was automated using a script developed in-house. The script performs cell detection using the nuclear marker DAPI and set the positivity for each marker using a threshold determined based on negative control samples. A cell classification tree was used to identify the phenotypes of interest. Cell counts for each phenotype were exported to a.csv file for further calculations to determine the percentage of each phenotype within a relevant population. An average of ~69,000 total cells were detected from 3 to 4 combined tumor cores per patient. Samples showing low total cell count (<25,000 cells from 3 to 4 combined cores) were excluded. The remaining 93 patient samples were further analyzed in Qupath using Kaplan Meier survival analysis to determine prognostic associations between the abundance of VISTA⁺ and/or ARG1⁺ tumor infiltrating CD11b⁺ or MDSC cells with disease-free and overall survival. Patients were initially stratified into “low” vs. “high” subgroups using the median abundance level as a cut-off, and subsequently, optimized cut-offs were determined using the Qupath survival analysis tool. For overall survival, the median abundance level was used to stratify “high” vs. “low” VISTA⁺/ARG1⁺/CD11b⁺ or MDSC subgroups (n = 46 vs. 47). For disease-free survival, the top 40th percentile abundance level was used to stratify “high” vs. “low” subgroups (n = 37 vs. 56). The survival curves were generated using GraphPad Prism (GraphPad Software, San Diego, California USA).

QUANTIFICATION AND STATISTICAL ANALYSIS

All graphs and statistical analysis were generated using Prism 7 (GraphPad Software, Inc., San Diego, CA). Unpaired two-tailed t tests were used for comparing the phenotypes between two independent groups. One-way ANOVA was used to compare the phenotypes between 3 independent groups. An unpaired two-tailed nonparametric Wilcoxon rank-sum test was used to compare tumor growth between WT (*Cx3cr1^{Cre/+}*) vs. conditional knockout (*Vsr^{fl/fl} Cx3cr1^{Cre/+}*) tumor-bearing mice and to analyze VISTA expression in human single-cell RNA-seq datasets. Survival differences were assessed using Kaplan-Meier curves and analyzed by log rank testing. All data were presented as mean \pm SEM. A p-value less than 0.05 is considered statistically significant. * $p < 0.05$; ** $p < 0.025$; *** $p < 0.005$; **** $p < 0.0001$. Statistical information about specific experiments can be found in the figure legends.

Supplementary Material

Refer to Web version on PubMed Central for supplementary material.

ACKNOWLEDGMENTS

We thank Sarah Stone for technical and administrative support. We thank Wei (Auston) Wei for statistical assistance. This work was supported by National Institute of Health/National Cancer Institute R01CA164225, R01CA223804, and R21CA258618 (to L.L.W.); Department of Defense CDMRP W81XWH-21-MRP-MCAA ME210229 and CDMRP W81XWH-21-LCRP-ITRA LC210336 (to L.L.W.); American Cancer Society RSG-18-045-01-LIB (to L.L.W.); The Norma C. and Albert I. Geller Professorship in Ovarian Cancer Research (to S.A.), a Case Comprehensive Cancer Center Genomics Pilot Grant (to S.A.); The V Foundation Scholar Award V2020-011 (to A.A.C.); Department of Defense Early Career Investigator Grant KCRP AKCI-ECI and W81XWH-20-1-0804 (to A.A.C.); an NCCN Young Investigator Award (to A.A.C.); American Cancer Society Research Scholar Grant RSG-22-067-01-TBE (to A.A.C.); American Cancer Society RSG-22-135-01-IBCD (to S.C.-C.H.); a Melanoma Research Foundation Career Development Award (to S.C.-C.H.); an Andrew McDonough B+ Foundation Grant Award (to S.C.-C.H.); Case GI SPORE DRP Grant 5P50CA150964-08 (to S.C.-C.H.); and a Cancer Research Institute CLIP Investigator Award (to S.C.-C.H.).

REFERENCES

1. Tcyganov E, Mastio J, Chen E, and Gabrilovich DI (2018). Plasticity of myeloid-derived suppressor cells in cancer. *Curr. Opin. Immunol* 51,76–82. [PubMed: 29547768]
2. Veglia F, Sanseviero E, and Gabrilovich DI (2021). Myeloid-derived suppressor cells in the era of increasing myeloid cell diversity. *Nat. Rev. Immunol* 21, 485–498. [PubMed: 33526920]
3. Hegde S, Leader AM, and Merad M (2021). MDSC: Markers, development, states, and unaddressed complexity. *Immunity* 54, 875–884. [PubMed: 33979585]
4. Goswami S, Anandhan S, Raychaudhuri D, and Sharma P. (2023). Myeloid cell-targeted therapies for solid tumours. *Nat. Rev. Immunol* 23, 106–120. [PubMed: 35697799]
5. Redd PS, Ibrahim ML, Klement JD, Sharman SK, Paschall AV, Yang D, Nayak-Kapoor A, and Liu K (2017). SETD1B Activates iNOS Expression in Myeloid-Derived Suppressor Cells. *Cancer Res.* 77, 2834–2843. [PubMed: 28381543]
6. Youn JI, Nagaraj S, Collazo M, and Gabrilovich DI (2008). Subsets of myeloid-derived suppressor cells in tumor-bearing mice. *J. Immunol* 131, 5791–5802.
7. Bian Z, Abdelaal AM, Shi L, Liang H, Xiong L, Kidder K, Venkataramani M, Culpepper C, Zen K, and Liu Y (2018). Arginase-1 is neither constitutively expressed in nor required for myeloid-derived suppressor cell-mediated inhibition of T-cell proliferation. *Eur. J. Immunol* 48, 1046–1058. [PubMed: 29488625]
8. Rodriguez PC, Quiceno DG, Zabaleta J, Ortiz B, Zea AH, Piazuelo MB, Delgado A, Correa P, Brayer J, Sotomayor EM, et al. (2004). Arginase I production in the tumor microenvironment

by mature myeloid cells inhibits T-cell receptor expression and antigen-specific T-cell responses. *Cancer Res.* 64, 5839–5849. [PubMed: 15313928]

9. Yu Z, Zhang W, and Kone BC (2002). Signal transducers and activators of transcription 3 (STAT3) inhibits transcription of the inducible nitric oxide synthase gene by interacting with nuclear factor kappaB. *Biochem. J* 367, 97–105. [PubMed: 12057007]
10. Mohamed E, Sierra RA, Trillo-Tinoco J, Cao Y, Innamarato P, Payne KK, de Mingo Pulido A, Mandula J, Zhang S, Thevenot P, et al. (2020). The Unfolded Protein Response Mediator PERK Governs Myeloid Cell-Driven Immunosuppression in Tumors through Inhibition of STING Signaling. *Immunity* 52, 668–682. [PubMed: 32294407]
11. Al-Khami AA, Zheng L, Del Valle L, Hossain F, Wyczzechowska D, Zabaleta J, Sanchez MD, Dean MJ, Rodriguez PC, and Ochoa AC (2017). Exogenous lipid uptake induces metabolic and functional reprogramming of tumor-associated myeloid-derived suppressor cells. *OncoImmunology* 6, e1344804. [PubMed: 29123954]
12. Hossain F, Al-Khami AA, Wyczzechowska D, Hernandez C, Zheng L, Reiss K, Valle LD, Trillo-Tinoco J, Maj T, Zou W, et al. (2015). Inhibition of Fatty Acid Oxidation Modulates Immunosuppressive Functions of Myeloid-Derived Suppressor Cells and Enhances Cancer Therapies. *Cancer Immunol. Res* 3, 1236–1247. [PubMed: 26025381]
13. Veglia F, Tyurin VA, Blasi M, De Leo A, Kossenkov AV, Donthireddy L, To TKJ, Schug Z, Basu S, Wang F, et al. (2019). Fatty acid transport protein 2 reprograms neutrophils in cancer. *Nature* 563, 73–78.
14. Wang L, Rubinstein R, Lines JL, Wasiuk A, Ahonen C, Guo Y, Lu LF, Gondek D, Wang Y, Fava RA, et al. (2011). VISTA, a novel mouse Ig superfamily ligand that negatively regulates T cell responses. *J. Exp. Med* 208, 577–592.
15. Xu W, Hi u T, Malarkannan S, and Wang L (2018). The structure, expression, and multifaceted role of immune-checkpoint protein VISTA as a critical regulator of anti-tumor immunity, autoimmunity, and inflammation. *Cell. Mol. Immunol* 15, 438–446. [PubMed: 29375120]
16. Flies DB, Han X, Higuchi T, Zheng L, Sun J, Ye JJ, and Chen L (2014). Coinhibitory receptor PD-1H preferentially suppresses CD4(+) T cell-mediated immunity. *J. Clin. Invest* 124, 1966–1975. [PubMed: 24743150]
17. Wang L, Le Mercier I, Putra J, Chen W, Liu J, Schenk AD, Nowak EC, Suriawinata AA, Li J, and Noelle RJ (2014). Disruption of the immune-checkpoint VISTA gene imparts a proinflammatory phenotype with predisposition to the development of autoimmunity. *Proc Natl Acad Sci USA* 111, 14846–14851. [PubMed: 25267631]
18. Strauss L, Mahmoud MAA, Weaver JD, Tijaro-Ovalle NM, Christofides A, Wang Q, Pal R, Yuan M, Asara J, Patsoukis N, and Boussiotis VA (2020). Targeted deletion of PD-1 in myeloid cells induces anti-tumor immunity. *Sci. Immunol* 5.
19. Johnston RJ, Su LJ, Pinckney J, Critton D, Boyer E, Krishnakumar A, Corbett M, Rankin AL, Dibella R, Campbell L, et al. (2019). VISTA is an acidic pH-selective ligand for PSGL-1. *Nature* 574, 565–570. [PubMed: 31645726]
20. Teft WA, Kirchhof MG, and Madrenas J (2006). A molecular perspective of CTLA-4 function. *Annu. Rev. Immunol* 24, 65–97. [PubMed: 16551244]
21. Hui E, Cheung J, Zhu J, Su X, Taylor MJ, Wallweber HA, Sasmal DK, Huang J, Kim JM, Mellman I, and Vale RD (2017). T cell costimulatory receptor CD28 is a primary target for PD-1-mediated inhibition. *Science* 355, 1428–1433. [PubMed: 28280247]
22. Le Mercier I, Chen W, Lines JL, Day M, Li J, Sargent P, Noelle RJ, and Wang L (2014). VISTA Regulates the Development of Protective Antitumor Immunity. *Cancer Res.* 74, 1933–1944. [PubMed: 24691994]
23. Liu J, Yuan Y, Chen W, Putra J, Suriawinata AA, Schenk AD, Miller HE, Guleria I, Barth RJ, Huang YH, and Wang L (2015). Immune-checkpoint proteins VISTA and PD-1 nonredundantly regulate murine T-cell responses. *Proc Natl Acad Sci USA* 112, 6682–6687. [PubMed: 25964334]
24. Xu W, Dong J, Zheng Y, Zhou J, Yuan Y, Ta HM, Miller HE, Olson M, Rajasekaran K, Ernstoff MS, et al. (2019). Immune-Checkpoint Protein VISTA Regulates Antitumor Immunity by Controlling Myeloid Cell-Mediated Inflammation and Immunosuppression. *Cancer Immunol. Res* 7, 1497–1510. [PubMed: 31340983]

25. Schaafsma E, Croteau W, ElTanbouly M, Nowak EC, Smits NC, Deng J, Sarde A, Webber CA, Rabadi D, Cheng C, et al. (2023). VISTA Targeting of T-cell Quiescence and Myeloid Suppression Overcomes Adaptive Resistance. *Cancer Immunol. Res* 11, 38–55. [PubMed: 36260656]
26. Deng J, Li J, Sarde A, Lines JL, Lee YC, Qian DC, Pechenick DA, Manivanh R, Le Mercier I, Lowrey CH, et al. (2019). Hypoxia-Induced VISTA Promotes the Suppressive Function of Myeloid-Derived Suppressor Cells in the Tumor Microenvironment. *Cancer Immunol. Res* 7, 1079–1090. [PubMed: 31088847]
27. Broughton TWK, ElTanbouly MA, Schaafsma E, Deng J, Sarde A, Croteau W, Li J, Nowak EC, Mabaera R, Smits NC, et al. (2019). Defining the Signature of VISTA on Myeloid Cell Chemokine Responsiveness. *Front. Immunol* 10, 2641. [PubMed: 31803182]
28. Marigo I, Bosio E, Solito S, Mesa C, Fernandez A, Dolcetti L, Ugel S, Sonda N, Biccianti S, Falisi E, et al. (2010). Tumor-induced tolerance and immune suppression depend on the C/EBPbeta transcription factor. *Immunity* 32, 790–802. [PubMed: 20605485]
29. Yaddanapudi K, Rendon BE, Lamont G, Kim EJ, Al Rayyan N, Richie J, Albeituni S, Waigel S, Wise A, and Mitchell RA (2016). MIF Is Necessary for Late-Stage Melanoma Patient MDSC Immune Suppression and Differentiation. *Cancer Immunol. Res* 4, 101–112. [PubMed: 26603621]
30. Haverkamp JM, Smith AM, Weinlich R, Dillon CP, Qualls JE, Neale G, Koss B, Kim Y, Bronte V, Herold MJ, et al. (2014). Myeloid-derived suppressor activity is mediated by monocytic lineages maintained by continuous inhibition of extrinsic and intrinsic death pathways. *Immunity* 41, 947–959. [PubMed: 25500368]
31. Groth C, Hu X, Weber R, Fleming V, Altevogt P, Utikal J, and Umansky V (2019). Immunosuppression mediated by myeloid-derived suppressor cells (MDSCs) during tumour progression. *Br. J. Cancer* 120, 16–25. [PubMed: 30413826]
32. Corzo CA, Condamine T, Lu L, Cotter MJ, Youn JI, Cheng P, Cho HI, Celis E, Quiceno DG, Padhya T, et al. (2010). HIF-1a regulates function and differentiation of myeloid-derived suppressor cells in the tumor microenvironment. *J. Exp. Med* 207, 2439–2453. [PubMed: 20876310]
33. Gabrilovich DI, and Nagaraj S (2009). Myeloid-derived suppressor cells as regulators of the immune system. *Nat. Rev. Immunol* 9, 162–174. [PubMed: 19197294]
34. Gough DJ, Koetz L, and Levy DE (2013). The MEK-ERK pathway is necessary for serine phosphorylation of mitochondrial STAT3 and Ras-mediated transformation. *PLoS One* 8, e83395. [PubMed: 24312439]
35. Wen Z, Zhong Z, and Darnell JE Jr. (1995). Maximal activation of transcription by Stat1 and Stat3 requires both tyrosine and serine phosphorylation. *Cell* 82, 241–250. [PubMed: 7543024]
36. Gough DJ, Corlett A, Schlessinger K, Wegrzyn J, Larner AC, and Levy DE (2009). Mitochondrial STAT3 supports Ras-dependent oncogenic transformation. *Science* 324, 1713–1716. [PubMed: 19556508]
37. Wegrzyn J, Potla R, Chwae YJ, Sepuri NBV, Zhang Q, Koeck T, Derecka M, Szczepanek K, Szelag M, Gornicka A, et al. (2009). Function of mitochondrial Stat3 in cellular respiration. *Science* 323, 793–797. [PubMed: 19131594]
38. Park JS, Woo MS, Kim SY, Kim WK, and Kim HS (2005). Repression of interferon-gamma-induced inducible nitric oxide synthase (iNOS) gene expression in microglia by sodium butyrate is mediated through specific inhibition of ERK signaling pathways. *J. Neuroimmunol* 168, 56–64. [PubMed: 16091294]
39. Chan ED, and Riches DW (2001). IFN-gamma + LPS induction of iNOS is modulated by ERK, JNK/SAPK, and p38(mapk) in a mouse macrophage cell line. *Am J. Physiol. Cell Physiol* 280, C441–C450. [PubMed: 11171562]
40. Vasquez-Dunddel D, Pan F, Zeng Q, Gorbounov M, Albesiano E, Fu J, Blosser RL, Tam AJ, Bruno T, Zhang H, et al. (2013). STAT3 regulates arginase-I in myeloid-derived suppressor cells from cancer patients. *J. Clin. Invest* 123, 1580–1589. [PubMed: 23454751]
41. Zhang G, He JL, Xie XY, and Yu C (2012). LPS-induced iNOS expression in N9 microglial cells is suppressed by geniposide via ERK, p38 and nuclear factor-kappaB signaling pathways. *Int. J. Mol. Med* 30, 561–568. [PubMed: 22710392]

42. Holbert CE, Cullen MT, Casero RA Jr., and Stewart TM (2022). Polyamines in cancer: integrating organismal metabolism and antitumour immunity. *Nat. Rev. Cancer* 22, 467–480. [PubMed: 35477776]
43. Proietti E, Rossini S, Grohmann U, and Mondanelli G (2020). Polyamines and Kynurenines at the Intersection of Immune Modulation. *Trends Immunol.* 41, 1037–1050. [PubMed: 33055013]
44. Bello-Fernandez C, Packham G, and Cleveland JL (1993). The ornithine decarboxylase gene is a transcriptional target of c-Myc. *Proc Natl Acad Sci USA* 90, 7804–7808. [PubMed: 8356088]
45. Kiuchi N, Nakajima K, Ichiba M, Fukada T, Narimatsu M, Mizuno K, Hibi M, and Hirano T (1999). STAT3 is required for the gp130-mediated full activation of the c-myc gene. *JJ. Exp. Med* 189, 63–73.
46. Rouillard AD, Gundersen GW, Fernandez NF, Wang Z, Monteiro CD, McDermott MG, and Ma'ayan A (2016). The harmonizome: a collection of processed datasets gathered to serve and mine knowledge about genes and proteins. *Database.*
47. Alexander ET, Mariner K, Donnelly J, Phanstiel O.t., and Gilmour SK (2020). Polyamine Blocking Therapy Decreases Survival of Tumor-Infiltrating Immunosuppressive Myeloid Cells and Enhances the Antitumor Efficacy of PD-1 Blockade. *Mol. Cancer Ther* 19, 2012–2022. [PubMed: 32747421]
48. Ye C, Geng Z, Dominguez D, Chen S, Fan J, Qin L, Long A, Zhang Y, Kuzel TM, and Zhang B (2016). Targeting Ornithine Decarboxylase by alpha-Difluoromethylornithine Inhibits Tumor Growth by Impairing Myeloid-Derived Suppressor Cells. *JJ. Immunol* 196, 915–923.
49. Cheng P, Kumar V, Liu H, Youn JI, Fishman M, Sherman S, and Gabrilovich D (2014). Effects of notch signaling on regulation of myeloid cell differentiation in cancer. *Cancer Res.* 74, 141–152. [PubMed: 24220241]
50. Hashimoto A, Gao C, Mastio J, Kossenkov A, Abrams SI, Purandare AV, Desilva H, Wee S, Hunt J, Jure-Kunkel M, and Gabrilovich DI (2018). Inhibition of Casein Kinase 2 Disrupts Differentiation of Myeloid Cells in Cancer and Enhances the Efficacy of Immunotherapy in Mice. *Cancer Res.* 78, 5644–5655. [PubMed: 30139814]
51. Leroy D, Heriché JK, Filhol O, Chambaz EM, and Cochet C (1997). Binding of polyamines to an autonomous domain of the regulatory subunit of protein kinase CK2 induces a conformational change in the holoenzyme. A proposed role for the kinase stimulation. *J. Biol. Chem* 272, 20820–20827. [PubMed: 9252407]
52. Zheng Y, Qin H, Frank SJ, Deng L, Litchfield DW, Tefferi A, Pardnani A, Lin FT, Li J, Sha B, and Benveniste EN (2011). A CK2-dependent mechanism for activation of the JAK-STAT signaling pathway. *Blood* 118, 156–166. [PubMed: 21527517]
53. Puleston DJ, Buck MD, Klein Geltink RI, Kyle RL, Caputa G, O'Sullivan D, Cameron AM, Castoldi A, Musa Y, Kabat AM, et al. (2019). Polyamines and eIF5A Hypusination Modulate Mitochondrial Respiration and Macrophage Activation. *Cell Metab* 30, 352–363.e358. [PubMed: 31130465]
54. Latour YL, Gobert AP, and Wilson KT (2020). The role of polyamines in the regulation of macrophage polarization and function. *Amino Acids* 52, 151–160. [PubMed: 31016375]
55. Pegg AE (2013). Toxicity of polyamines and their metabolic products. *Chem. Res. Toxicol* 26, 1782–1800. [PubMed: 24224555]
56. Murray Stewart T, Dunston TT, Woster PM, and Casero RA Jr. (2018). Polyamine catabolism and oxidative damage. *J. Biol. Chem* 293, 18736–18745. [PubMed: 30333229]
57. Davidov V, Jensen G, Mai S, Chen SH, and Pan PY (2020). Analyzing One Cell at a TIME: Analysis of Myeloid Cell Contributions in the Tumor Immune Microenvironment. *Front. Immunol* 11, 1842. [PubMed: 32983100]
58. Jung S, Aliberti J, Graemmel P, Sunshine MJ, Kreutzberg GW, Sher A, and Littman DR (2000). Analysis of fractalkine receptor CX(3) CR1 function by targeted deletion and green fluorescent protein reporter gene insertion. *Mol. Cell. Biol* 20, 4106–4114. [PubMed: 10805752]
59. Yona S, Kim KW, Wolf Y, Mildner A, Varol D, Breker M, Strauss-Ayali D, Viukov S, Guillems M, Misharin A, et al. (2013). Fate mapping reveals origins and dynamics of monocytes and tissue macrophages under homeostasis. *Immunity* 38, 79–91. [PubMed: 23273845]

60. Schultze JL, Mass E, and Schlitzer A (2019). Emerging Principles in Myelopoiesis at Homeostasis and during Infection and Inflammation. *Immunity* 50, 288–301. [PubMed: 30784577]
61. Buechler MB, Teal TH, Elkon KB, and Hamerman JA (2013). Cutting edge: Type I IFN drives emergency myelopoiesis and peripheral myeloid expansion during chronic TLR7 signaling. *J. Immunol* 190, 886–891.
62. Yadav M, Jhunjunwala S, Phung QT, Lupardus P, Tanguay J, Bumbaca S, Franci C, Cheung TK, Fritsche J, Weinschenk T, et al. (2014). Predicting immunogenic tumour mutations by combining mass spectrometry and exome sequencing. *Nature* 515, 572–576. [PubMed: 25428506]
63. Hos BJ, Camps MGM, van den Bulk J, Tondini E, van den Ende TC, Ruano D, Franken K, Janssen GMC, Ru A, Filippov DV, et al. (2019). Identification of a neo-epitope dominating endogenous CD8 T cell responses to MC-38 colorectal cancer. *OncoImmunology* 9, 1673125. [PubMed: 32923109]
64. Mastio J, Condamine T, Dominguez G, Kossenkov AV, Donthireddy L, Veglia F, Lin C, Wang F, Fu S, Zhou J, et al. (2019). Identification of monocyte-like precursors of granulocytes in cancer as a mechanism for accumulation of PMN-MDSCs. *J. Exp. Med* 216, 2150–2169.
65. Cerami E, Gao J, Dogrusoz U, Gross BE, Sumer SO, Aksoy BA, Jacobsen A, Byrne CJ, Heuer ML, Larsson E, et al. (2012). The cBio cancer genomics portal: an open platform for exploring multidimensional cancer genomics data. *Cancer Discov.* 2, 401–404. [PubMed: 22588877]
66. Gao J, Aksoy BA, Dogrusoz U, Dresdner G, Gross B, Sumer SO, Sun Y, Jacobsen A, Sinha R, Larsson E, et al. (2013). Integrative analysis of complex cancer genomics and clinical profiles using the cBioPortal. *Sci. Signal* 6, pii. [PubMed: 23550210]
67. Sade-Feldman M, Yizhak K, Bjorgaard SL, Ray JP, de Boer CG, Jenkins RW, Lieb DJ, Chen JH, Frederick DT, Barzily-Rokni M, et al. (2019). Defining T Cell States Associated with Response to Checkpoint Immunotherapy in Melanoma. *Cell* 176, 404. [PubMed: 30633907]
68. Alshetaiwi H, Pervolarakis N, McIntyre LL, Ma D, Nguyen Q, Rath JA, Nee K, Hernandez G, Evans K, Torosian L, et al. (2020). Defining the emergence of myeloid-derived suppressor cells in breast cancer using single-cell transcriptomics. *Sci. Immunol* 5.
69. Youn JI, and Gabrilovich DI (2010). The biology of myeloid-derived suppressor cells: the blessing and the curse of morphological and functional heterogeneity. *Eur. J. Immunol* 40, 2969–2975. [PubMed: 21061430]
70. Kwak T, Wang F, Deng H, Condamine T, Kumar V, Perego M, Kossenkov A, Montaner LJ, Xu X, Xu W, et al. (2020). Distinct Populations of Immune-Suppressive Macrophages Differentiate from Monocytic Myeloid-Derived Suppressor Cells in Cancer. *Cell Rep.* 33, 108571. [PubMed: 33378668]
71. Garama DJ, White CL, Balic JJ, and Gough DJ (2016). Mitochondrial STAT3: Powering up a potent factor. *Cytokine* 87, 20–25. [PubMed: 27269970]
72. Poli V, and Camporeale A (2015). STAT3-Mediated Metabolic Reprograming in Cellular Transformation and Implications for Drug Resistance. *Front. Oncol* 5, 121. [PubMed: 26106584]
73. Lee M, Hirpara JL, Eu JQ, Sethi G, Wang L, Goh BC, and Wong AL (2019). Targeting STAT3 and oxidative phosphorylation in oncogene-addicted tumors. *Redox Biol.* 25, 101073. [PubMed: 30594485]
74. Al-Habsi M, Chamoto k., Matsumoto K, Nomura N, Zhang B, Sugiura Y, Sonomura K, Maharani A, Nakajima Y, Wu Y, et al. (2022). Spermidine activates mitochondrial trifunctional protein and improves antitumor immunity in mice. *Science* 378, eabj3510. [PubMed: 36302005]
75. Pasini A, Caldarella CM, and Giordano E (2014). Chromatin remodeling by polyamines and polyamine analogs. *Amino Acids* 46, 595–603. [PubMed: 23836422]
76. Kumar V, Patel S, Tcyganov E, and Gabrilovich DI (2016). The Nature of Myeloid-Derived Suppressor Cells in the Tumor Microenvironment. *Trends Immunol.* 37, 208–220. [PubMed: 26858199]
77. Santini SM, Lapenta C, Logozzi M, Parlato S, Spada M, Di Pucchio T, and Belardelli F (2000). Type I interferon as a powerful adjuvant for monocyte-derived dendritic cell development and activity in vitro and in Hu-PBL-SCID mice. *J. Exp. Med* 191, 1777–1788.

78. Nefedova Y, Huang M, Kusmartsev S, Bhattacharya R, Cheng P, Salup R, Jove R, and Gabrilovich D (2004). Hyperactivation of STAT3 is involved in abnormal differentiation of dendritic cells in cancer. *J. Immunol* 172, 464–474.
79. Park SJ, Nakagawa T, Kitamura H, Atsumi T, Kamon H, Sawa SI, Kamimura D, Ueda N, Iwakura Y, Ishihara K, et al. (2004). IL-6 regulates in vivo dendritic cell differentiation through STAT3 activation. *J. Immunol* 173, 3844–3854.
80. Melillo JA, Song L, Bhagat G, Blazquez AB, Plumlee CR, Lee C, Berin C, Reizis B, and Schindler C (2010). Dendritic cell (DC)-specific targeting reveals Stat3 as a negative regulator of DC function. *J. Immunol* 184, 2638–2645.
81. Kitamura H, Kamon H, Sawa S, Park SJ, Katunuma N, Ishihara K, Murakami M, and Hirano T (2005). IL-6-STAT3 controls intracellular MHC class II alphabeta dimer level through cathepsin S activity in dendritic cells. *Immunity* 23, 491–502. [PubMed: 16286017]
82. Barry ST, Gabrilovich DI, Sansom OJ, Campbell AD, and Morton JP (2023). Therapeutic targeting of tumour myeloid cells. *Nat. Rev. Cancer* 23, 216–237. [PubMed: 36747021]
83. Jian SL, Chen WW, Su YC, Su YW, Chuang TH, Hsu SC, and Huang LR (2017). Glycolysis regulates the expansion of myeloid-derived suppressor cells in tumor-bearing hosts through prevention of ROS-mediated apoptosis. *Cell Death Dis.* 8, e2779. [PubMed: 28492541]
84. Mohammadpour H, MacDonald CR, McCarthy PL, Abrams SI, and Repasky EA (2021). beta2-adrenergic receptor signaling regulates metabolic pathways critical to myeloid-derived suppressor cell function within the TME. *Cell Rep.* 37, 109883. [PubMed: 34706232]
85. Yoon KW, Byun S, Kwon E, Hwang SY, Chu K, Hiraki M, Jo SH, Weins A, Hakrout S, Cebulla A, et al. (2015). Control of signaling-mediated clearance of apoptotic cells by the tumor suppressor p53. *Science* 349, 1261669. [PubMed: 26228159]
86. Yuan M, Breitkopf SB, Yang X, and Asara JM (2012). A positive/negative ion-switching, targeted mass spectrometry-based metabolomics platform for bodily fluids, cells, and fresh and fixed tissue. *Nat. Protoc* 7, 872–881. [PubMed: 22498707]
87. Pang Z, Chong J, Zhou G, de Lima Morais DA, Chang L, Barrette M, Gauthier C, Jacques PÉ, Li S, and Xia J (2021). MetaboAnalyst 5.0: narrowing the gap between raw spectra and functional insights. *Nucleic Acids Res.* 49, W388–W396. [PubMed: 34019663]
88. Zhao J, Jaffe A, Li H, Lindenbaum O, Sefik E, Jackson R, Cheng X, Flavell RA, and Kluger Y (2021). Detection of differentially abundant cell subpopulations in scRNA-seq data. *Proc. Natl. Acad. Sci. USA* 118.
89. Cao L, Huang C, Cui Zhou D, Hu Y, Lih TM, Savage SR, Krug K, Clark DJ, Schnaubelt M, Chen L, et al. (2021). Proteogenomic characterization of pancreatic ductal adenocarcinoma. *Cell* 184, 5031–5052. [PubMed: 34534465]
90. Dou Y, Kawaler EA, Cui Zhou D, Gritsenko MA, Huang C, Blumenberg L, Karpova A, Petyuk VA, Savage SR, Satpathy S, et al. (2020). Proteogenomic Characterization of Endometrial Carcinoma. *Cell* 180, 729–748. [PubMed: 32059776]
91. Gillette MA, Satpathy S, Cao S, Dhanasekaran SM, Vasaikar SV, Krug K, Petralia F, Li Y, Liang WW, Reva B, et al. (2020). Proteogenomic Characterization Reveals Therapeutic Vulnerabilities in Lung Adenocarcinoma. *Cell* 182, 200–225. [PubMed: 32649874]
92. Liu D, Schilling B, Liu D, Sucker A, Livingstone E, Jerby-Aron L, Zimmer L, Gutzmer R, Satzger I, Loquai C, et al. (2019). Integrative molecular and clinical modeling of clinical outcomes to PD1 blockade in patients with metastatic melanoma. *Nat. Med* 25, 1916–1927. [PubMed: 31792460]
93. Besson S, Leigh R, Linkert M, Allan C, Burel JM, Carroll M, Gault D, Gozim R, Li S, Lindner D, et al. (2019). Bringing Open Data to Whole Slide Imaging. *Digit. Pathol* 2019, 3–10.
94. Linkert M, Rueden CT, Allan C, Burel JM, Moore W, Patterson A, Loranger B, Moore J, Neves C, Macdonald D, et al. (2010). Metadata matters: access to image data in the real world. *J. Cell Biol* 189, 777–782. [PubMed: 20513764]
95. Goldberg IG, Allan C, Burel JM, Creager D, Falconi A, Hochheiser H, Johnston J, Mellen J, Sorger PK, and Swedlow JR (2005). The Open Microscopy Environment (OME) Data Model and XML file: open tools for informatics and quantitative analysis in biological imaging. *Genome Biol.* 6, R47. [PubMed: 15892875]

96. Bankhead P, Loughrey MB, Fernández JA, Dombrowski Y, McArt DG, Dunne PD, McQuaid S, Gray RT, Murray LJ, Coleman HG, et al. (2017). QuPath: Open source software for digital pathology image analysis. *Sci. Rep* 7, 16878. [PubMed: 29203879]

Author Manuscript

Author Manuscript

Author Manuscript

Author Manuscript

Highlights

- VISTA drives MDSC differentiation by sustaining STAT3 activation and polyamine biosynthesis
- VISTA promotes MDSC mitochondrial respiration in STAT3- and polyamine-dependent manner
- Blocking VISTA in monocytic progenitors improved antitumor immune responses
- Correlated expression of VISTA and ARG1 in myeloid cells is prognostic in endometrial cancer

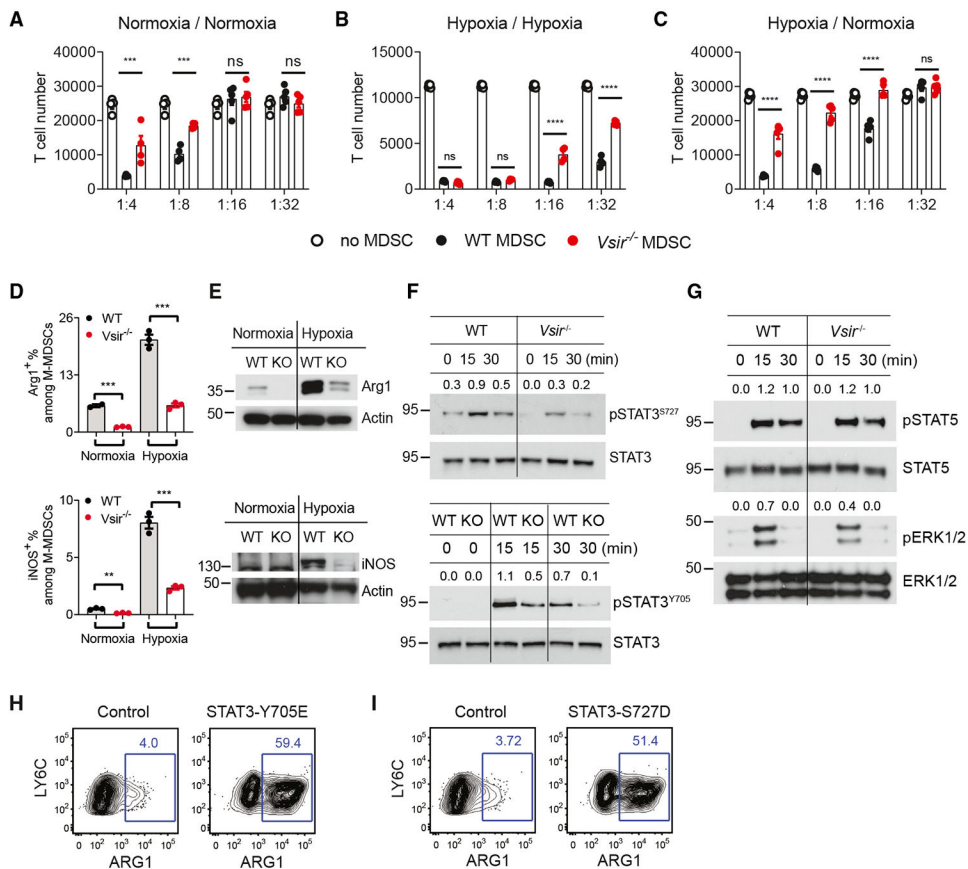


Figure 1. VISTA regulates the suppressive function of MDSCs by promoting STAT3 activation and the expression of Arg1 and iNOS

WT and *Vsir*^{-/-} BM progenitor cells were cultured with GM-CSF (10 ng/mL) and IL-6 (10 ng/mL) for 4 days either in normoxia or exposed to hypoxia during the last 24 h. M-MDSCs (Ly6C⁺Ly6G^{neg} CD11c^{neg}) were purified and cocultured with OT1 splenocytes (50,000) at the indicated ratios in the presence of the ovalbumin peptide (SIINFEKL, 100 μg/mL). Expanded OT1 T cells were enumerated by flow cytometry after 72 h of stimulation.

(A) Normoxic M-MDSCs and OT1 cells were co-cultured under normoxia for 72 h (n = 4 replicates).

(B) Hypoxic M-MDSCs and OT1 cells were continuously co-cultured under hypoxia for 72 h (n = 4 replicates).

(C) Hypoxic M-MDSCs were co-cultured with OT1 cells under normoxia for 72 h (n = 4 replicates).

(D and E) Protein expression of Arg1 and iNOS in normoxic or hypoxic M-MDSCs after 4-day culture was examined by flow cytometry (n = 3 replicates) and by western blotting.

(F) Hypoxic WT and *Vsir*^{-/-} M-MDSCs were rested for 8 h in medium without any cytokines and restimulated with IL-6. Cells were lysed at the indicated time points. Phosphorylated and total levels of STAT3 were detected by western blotting.

(G) Hypoxic WT and *Vsir*^{-/-} M-MDSCs were rested for 8 h and restimulated with GM-CSF. Cell lysates were generated and examined for phosphorylated and total levels of STAT5 and ERK1/2. The ratios of phosphorylated vs. total proteins were quantified using ImageJ.

(H and I) *Vsir*^{-/-} BM progenitor cells were transduced with a retrovirus expressing the mutant STAT3 proteins Y705E.GFP and S727D.GFP as indicated. Cells were expanded in GM-CSF and IL-6 for 4 days, and the expression of Arg1 was examined by flow cytometry. GFP^{neg} cells that did not express the mutant STAT3 are shown as parallel negative controls. All data were presented as mean ± SEM. * p < 0.05; ** p < 0.025; *** p < 0.005; **** p < 0.0001. All experiments were repeated at least three times, and representative results are shown.

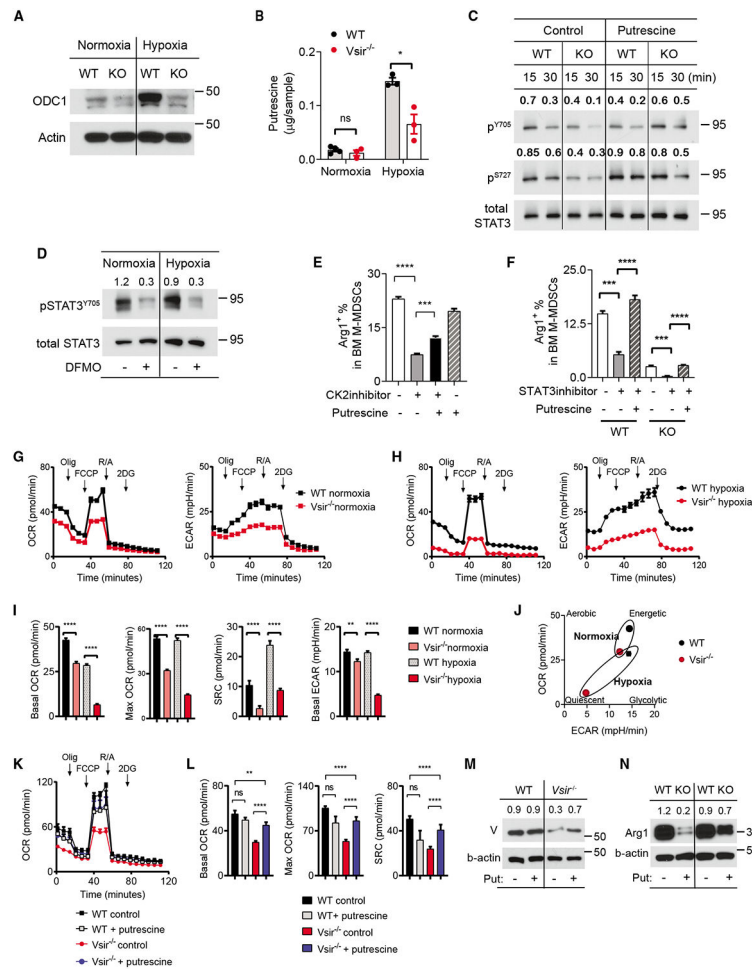


Figure 2. VISTA promotes polyamine biosynthesis and sustains Arg1 expression and mitochondrial functions partly in a STAT3- and polyamine-dependent manner

(A and B) WT and *Vsir*^{-/-} BM-derived MDSCs were cultured with GM-CSF and IL-6 for 4 days either in normoxia or exposed to hypoxia during the last 24 h. Total cell lysates were extracted and examined for ODC1 expression (A). Intracellular putrescine levels were quantified by liquid chromatography-tandem mass spectrometry (LC-MS/MS) (B) (n = 4 for normoxia replicates, n = 3 for hypoxia replicates).

(C) Hypoxic WT and *Vsir*^{-/-} MDSCs were cultured as in (A) in the presence of putrescine (800 μ M) or vehicle control. Cells were rested for 8 h before being restimulated with IL-6. Total cell lysates were examined by western blotting. The ratios of phosphorylated-STAT3^{Y705} and STAT3^{S727} vs. total STAT3 were quantified using ImageJ.

(D) WT BM-derived MDSCs were cultured as in (A) in the presence of DFMO (400 μ M) or vehicle control for 4 days. Total cell lysates were generated, and levels of pSTAT3^{Y705} and total STAT3 were examined by western blotting.

(E) WT BM progenitors (n = 3) were cultured for 4 days as in (A). On day +1, CK2 inhibitor (20 μ M), putrescine (800 μ M), vehicle control, or combined drugs were added to the culture medium and continuously cultured for another 3 days. During the last 24 h, cells were treated with hypoxia before flow analysis to detect Arg1 expression.

(F) WT and *Vsir*^{-/-} BM-MDSCs (n = 3) were cultured for 4 days as in (A). On day +1, STAT3 inhibitor (2 mM), putrescine (1 mM), vehicle control, or combined drugs were added to the culture medium. Cells were treated with hypoxia during the last 24 h before flow analysis. All experiments were repeated at least three times, and representative results are shown.

(G and H) WT and *Vsir*^{-/-} BM-MDSCs were cultured for 4 days under normoxia or exposed to hypoxia during the last 24 h. Mitochondrial respiration of normoxic (G) and hypoxic MDSCs (H) was examined using the Seahorse XF Cell Mito stress test. The OCR and ECAR were recorded simultaneously.

(I) Basal OCR, maximal OCR, SRC, and ECAR are summarized.

(J) The bioenergetic profiles of WT and *Vsir*^{-/-} MDSCs were plotted based on basal OCR and ECAR levels.

(K and L) To rescue the defective mitochondrial function in *Vsir*^{-/-} MDSCs, putrescine (800 μ M) was added to the culture medium on day +1. Cells were cultured for a total of 4 days and treated with hypoxia during the last 24 h. M-MDSCs were purified and examined using the Mito stress test. OCR was recorded (K). Basal OCR, maximal OCR, and SRC are summarized (L).

(M and N) Total cell lysates were extracted, and the expression of ETC complex V and Arg1 was examined. β -Actin was used as the loading control. The ratios of each protein vs. β -actin were quantified using ImageJ. All experiments were repeated at least three times, and representative results are shown.

Statistical analysis: n = 8 (WT, normoxia), 9 (KO, normoxia), 8 (WT, hypoxia), and 10 (KO, hypoxia) replicates (A–C); n = 5 (WT control), 4 (WT putrescine), 14 (KO, control), and 8 (KO putrescine) replicates (D). All data were presented as mean \pm SEM. * p < 0.05; ** p < 0.025; *** p < 0.005; **** p < 0.0001.

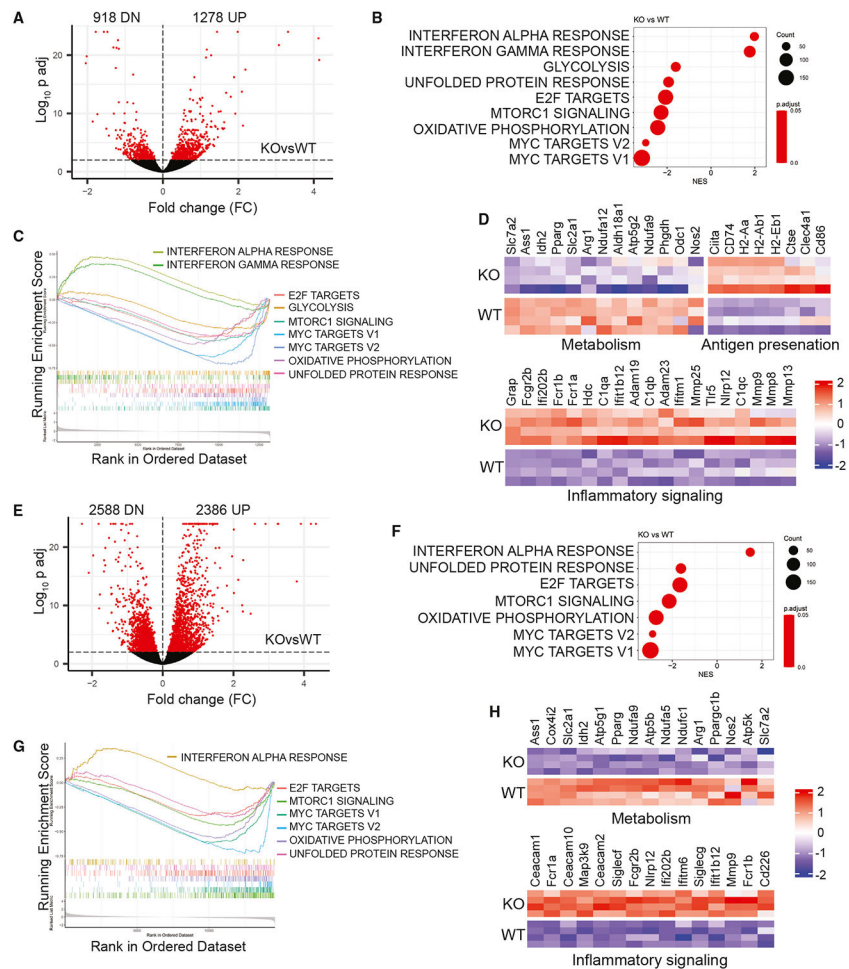


Figure 3. VISTA-dependent molecular pathways govern the metabolism, cell growth, and responses to inflammatory stimuli in M-MDSCs

WT and *Vsir*^{-/-} BM-derived M-MDSCs (n = 4) were cultured for 4 days, either under normoxia (A–D) or exposed to hypoxia during the last 24 h (E–H). Total RNA was extracted and analyzed by RNA-seq. The volcano plots demonstrate the numbers of DEGs in normoxic (A) and hypoxic (E) *Vsir*^{-/-} MDSCs. GSEAs revealed molecular pathways that were significantly upregulated or downregulated in *Vsir*^{-/-} normoxic (B and C) and hypoxic (F and G) M-MDSCs. Shown are enrichment values of significantly altered pathways and graphic views of the leading-edge enrichment plots. Expression of a select list of genes that regulate antigen presentation, inflammatory signaling, and metabolism in normoxic (D) and hypoxic (H) M-MDSCs is shown.

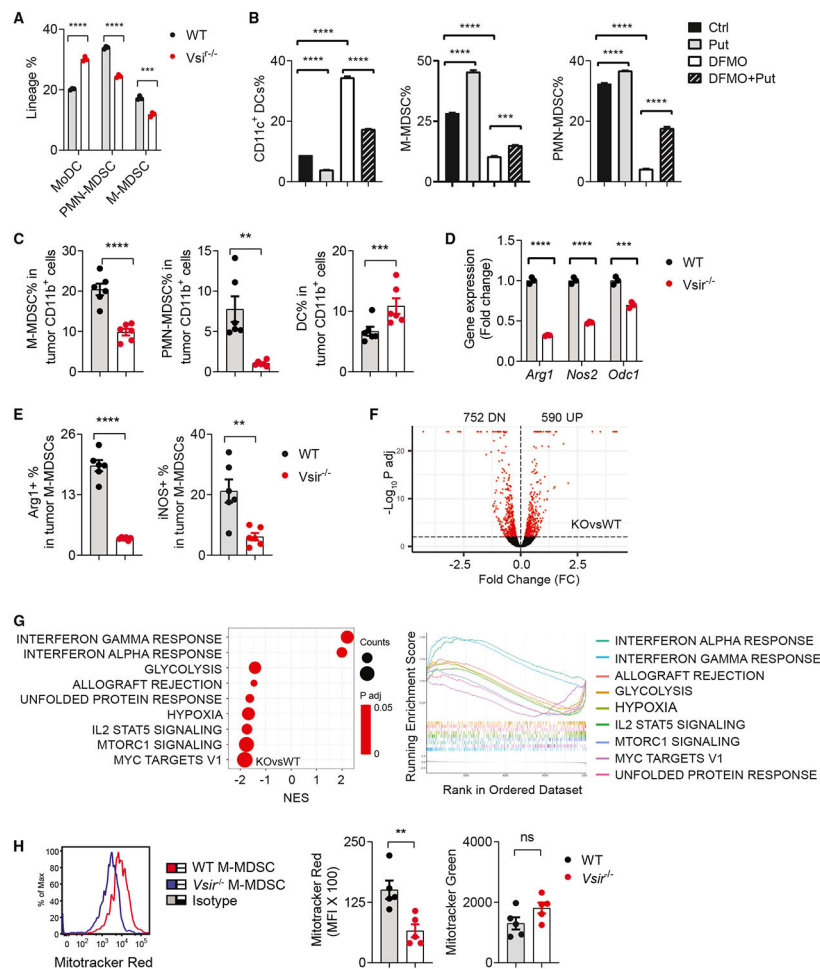


Figure 4. VISTA deficiency impaired the differentiation of tumor-associated MDSCs while expanding moDCs.

(A) WT and *Vsir*^{-/-} BM progenitor cells (n = 3) were cultured with GM-CSF and IL-6 for 5 days and exposed to hypoxia during the last 24 h. Nonadherent and adherent cells were harvested and pooled. MoDCs (CD11b⁺CD11c⁺MHCII⁺), M-MDSCs (CD11b⁺CD11c^{neg}Ly6C⁺Ly6G^{neg}), and PMN-MDSCs (CD11b⁺CD11c^{neg}Ly6C⁺Ly6G⁺) were examined by flow cytometry.

(B) WT BM progenitor cells (n = 3) were cultured as in (A). On day +1, putrescine (800 μ M), DFMO (400 μ M), or combined drugs were added to the culture medium. Cells were exposed to hypoxia during the last 24 h before being harvested and examined by flow cytometry.

(C–E) WT (CD45.1) and *Vsir*^{-/-} (CD45.2) mixed BM chimera mice were inoculated with MC38 colon cancer cells (1×10^6). Tumor tissues were harvested when tumors reached 8–9 mm in diameter (around day 18). Tumor-associated M-MDSCs (CD11b⁺Ly6C^{hi}CD11c^{neg}Ly6G^{neg}), PMN-MDSCs (CD11b⁺Ly6C^{lo}CD11c^{neg}Ly6G⁺), and moDCs (CD11b⁺CD11c^{hi} MHC class II⁺) were detected by flow cytometry. Percentages of each subset among the total CD11b⁺ myeloid cells are shown (C) (n = 6). Gene expression of *Arg1*, *nos2*, and *Odc1* in purified M-MDSCs was analyzed by RT-qPCR (D) (n = 3).

Protein expression of Arg1 and iNOS in M-MDSCs was examined by flow cytometry (E) (n = 6).

(F and G) Transcriptomic analyses of WT and *Vsir*^{-/-} tumor-associated M-MDSCs. Numbers of DEGs are illustrated in volcano plots (F). GSEAs revealed molecular pathways that were significantly upregulated or downregulated in *Vsir*^{-/-} tumor M-MDSCs. Normalized enrichment scores (NESs) and a graphic view of the leading edge enrichment plot are shown (G).

(H) Tumor-associated M-MDSCs from the BM chimera mice were stained with MitoTracker Green and Deep Red and examined by flow cytometry (n = 5).

All data were presented as mean ± SEM. * p < 0.05; ** p < 0.025; *** p < 0.005; **** p < 0.0001. All experiments were repeated at least two or three times, and representative results are shown.

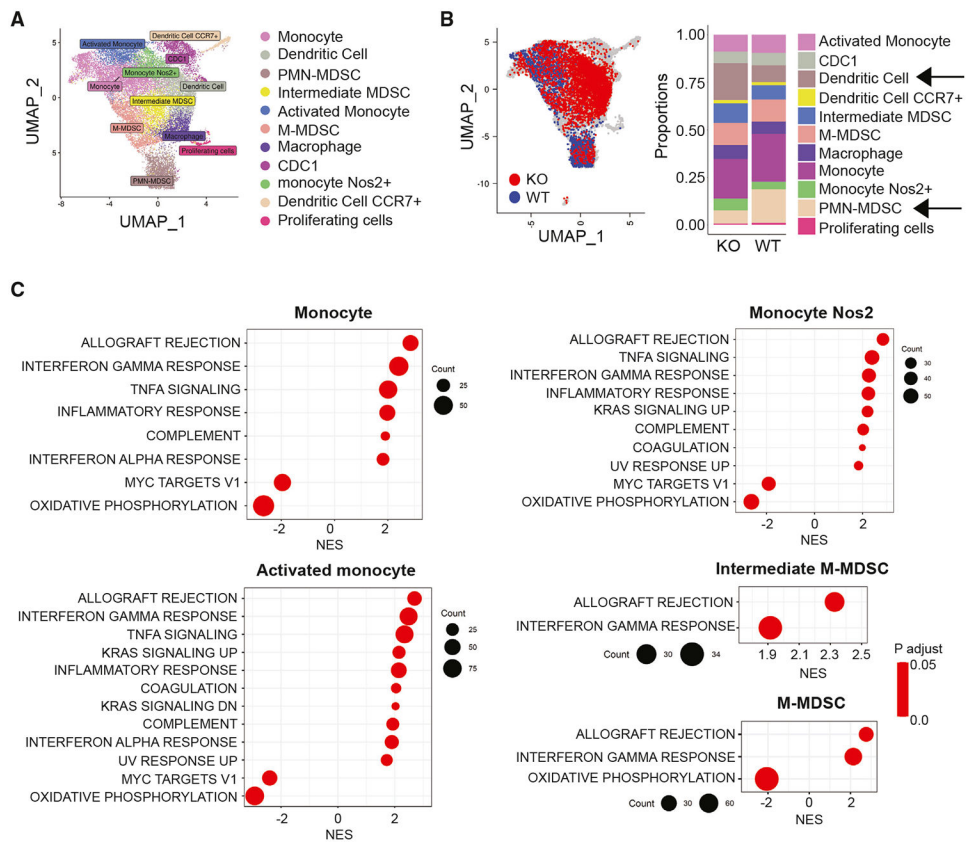


Figure 5. Single-cell transcriptomic analyses revealed that VISTA regulates inflammatory signaling and mitochondrial function in multiple tumor-associated monocytic cell subsets Tumor-associated WT (CD45.1) and *Vsirr*^{-/-} (CD45.2) myeloid cells (CD11b⁺) were sorted from mixed BM chimera mice bearing MC38 tumors (pooled from 10 tumors with 8- to 9-mm diameters) and subjected to single-cell transcriptomic profiling.

(A) UMAP clusters of tumor-associated CD11b⁺ myeloid cells.

(B) Cluster differential abundance analysis revealed that *Vsirr*^{-/-} cells (red) were more abundant in the “DC” and “Monocyte_Nos2” clusters, whereas WT cells (blue) were significantly more abundant in the “PMN-MDSC” cluster.

(C) GSEAs of individual myeloid clusters revealed molecular pathways that were upregulated or downregulated in *Vsirr*^{-/-} monocytic cells, including “Monocyte,” “Activated monocytes,” “Monocyte_Nos2,” “Intermediate M-MDSC,” and “M-MDSC” cells.

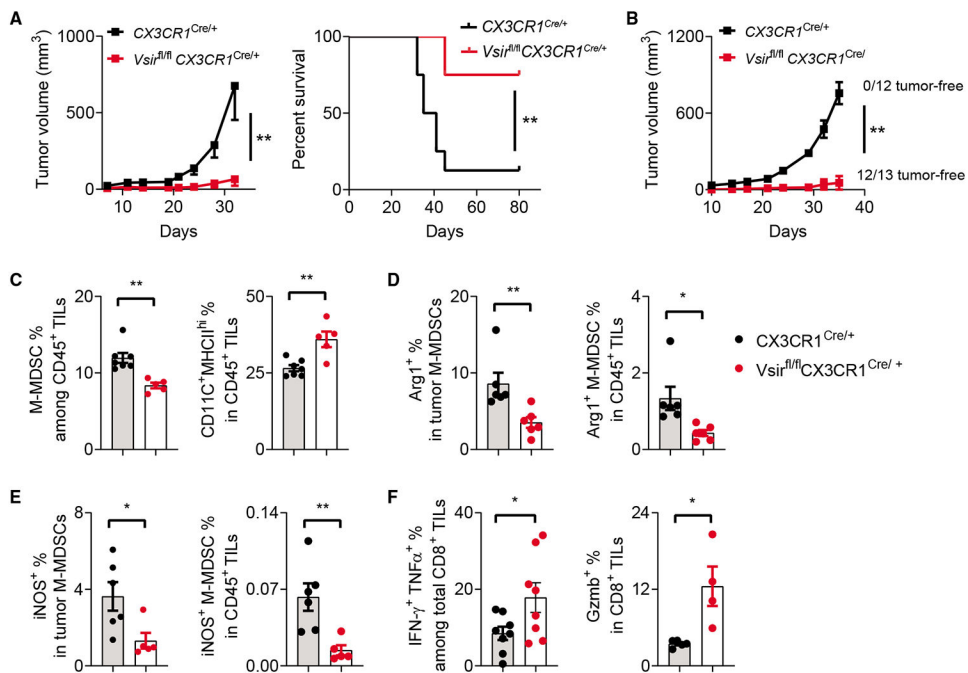


Figure 6. Myeloid-specific VISTA deficiency reduced MDSC abundance and augmented anti-tumor T cell responses

Myeloid-specific VISTA conditional KO mice ($Vsif^{fl/fl}Cx3CR1^{Cre/+}$) and WT littermates ($Cx3CR1^{Cre/+}$) (n = 8) were inoculated with MC38 tumor cells (100,000) on day 0. Mice were treated with a peptide vaccine containing CpG/R848 adjuvants on day 3. Tumor size was monitored with calipers every 2–3 days.

(A) Tumor growth curve and tumor-free survival (n = 8).

(B) $Vsif^{fl/fl} Cx3CR1^{Cre/+}$ mice that survived and remained tumor-free for 80 days were re-challenged with MC38 tumors (50,000) and monitored for secondary tumor growth (n = 12). Naive KO mice (n = 13) were examined as parallel controls.

(C–F) To investigate the phenotypes of tumor-infiltrating immune cells, mice bearing MC38 tumors were treated with a reduced vaccine dose. Tumor tissues were harvested on day 14, when most of the WT tumors reached more than 9 mm in diameter. M-MDSCs and moDCs within CD45⁺ tumor-infiltrating lymphocytes (TILs) were detected by flow cytometry (C). The expression of Arg1 (D) and iNOS (E), cytokines (IFN- γ and TNF- α), and granzyme B in T cells (F) was examined by flow cytometry.

Statistical analysis: n = 7 (WT) and 5 (KO) tumors (C); n = 6 (WT) and 6 (KO) tumors (D); n = 6 (WT) and 5 (KO) tumors (E); n = 8 (WT) and 8 (KO) tumors (F, cytokine) and n = 5 (WT) and 4 (KO) tumors (F, granzyme B). All data were presented as mean \pm SEM. * p < 0.05; ** p < 0.025; *** p < 0.005; **** p < 0.0001. All experiments were repeated at least two times, and representative results are shown.

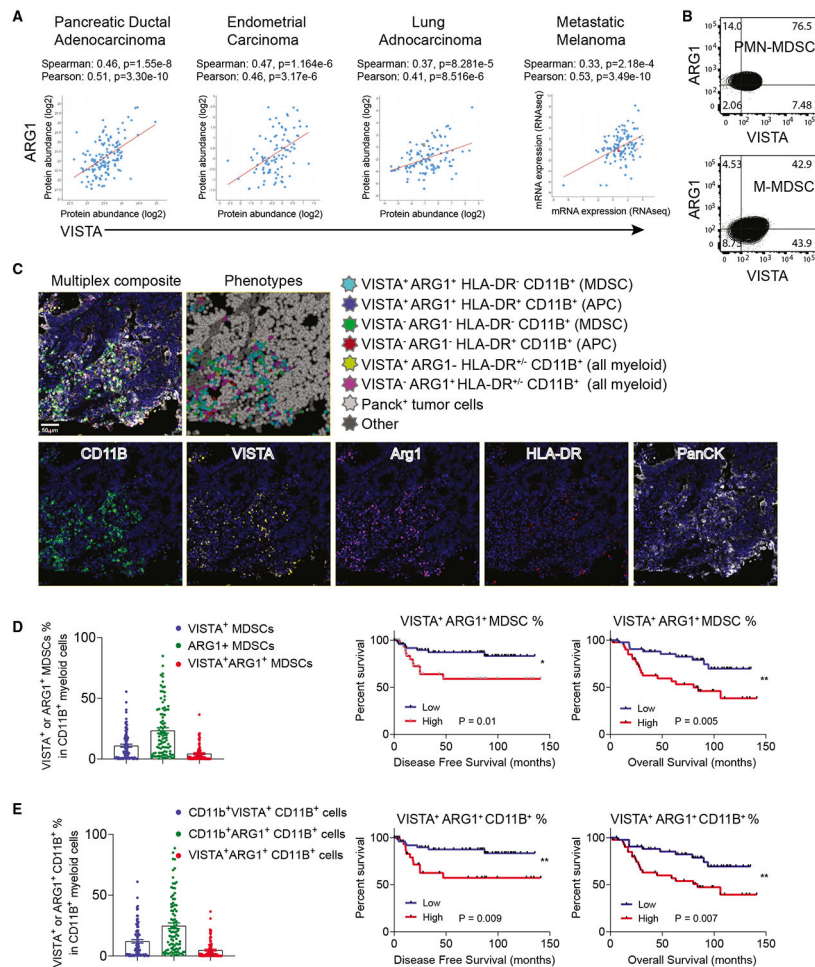


Figure 7. Expression of VISTA and ARG1 in human cancers and their prognostic association with poor survival in endometrial cancer

(A) Expression of VISTA and ARG1 was investigated in the cBioPortal for Cancer Genomics (<http://cbioportal.org>). Correlated protein expression of VISTA and ARG1 was shown in studies of pancreatic ductal adenocarcinoma, endometrial carcinoma, and lung adenocarcinoma. Correlated gene expression (mRNA levels) of VISTA and ARG1 was shown in a study of metastatic melanoma.

(B) Expression of VISTA and ARG1 in human endometrial tumor-associated PMN-MDSCs (CD11B⁺HLA-DR^{low}CD33⁺CD15⁺) and M-MDSCs (CD11B⁺HLA-DR^{int}CD33⁺CD14⁺) was examined by flow cytometry.

(C–E) Multiplexed IF analyses were performed on an endometrial cancer TMA (n = 93). Tumor-associated MDSCs (CD11B⁺HLA-DR^{neg}), APCs (CD11B⁺HLA-DR⁺), or total myeloid populations (CD11B⁺) were identified based on marker expression. An example of cell phenotype stratification is shown in (C). Numbers of VISTA/ARG1-expressing MDSCs (D) or total myeloid cells (E) were enumerated, and their percentages among the total CD11B⁺ myeloid populations were calculated and associated with DFS and OS.

KEY RESOURCES TABLE

REAGENT or RESOURCE	SOURCE	IDENTIFIER
Antibodies		
Anti-mouse CD45.1	Biologend	Clone A20
Anti-mouse CD45.2	Biologend	Clone 104
Anti-mouse CD11b	Biologend	Clone M1/70
Anti-mouse CD11C	Biologend	Clone N418
Anti-mouse Ly6C	Biologend	Clone HK1.4
Anti-mouse Ly6G	Biologend	Clone 1A8
Anti-mouse Arg1	Biologend	Clone AlexF5
Anti-mouse iNOS	Biologend	Clone CXNFT
Anti-mouse MHCII	Biologend	Clone M5/114.15.2
Anti-mouse VISTA	Biologend	Clone MIH63; RRID:AB_2566412
Anti-mouse c-Kit	Biologend	Clone 2B8
Anti-mouse Sca-1	Biologend	Clone D7
Anti-mouse CD4	Biologend	Clone RM4-5
Anti-mouse CD8	Biologend	Clone 53-6.7
Anti-mouse CD3	Biologend	Clone 145-2c11
Anti-mouse B220	Biologend	Clone RA3-6B2
Anti-mouse NK1.1	Biologend	Clone PK136
Anti-mouse F4/80	Biologend	Clone BM8
Anti-mouse CD11c	Biologend	Clone N418
anti-CD16/32 FCR blocker	Biologend	101319; RRID:AB_1574973
Anti-mouse Arg1	Cell Signaling Technology	93668S; RRID:AB_2800207
Anti-mouse ODC1	Cell Signaling Technology	28728-1-AP
Anti-mouse iNOS	Cell Signaling Technology	13120S; RRID:AB_2687529
Mouse p-STAT3	Cell Signaling Technology	9145S; RRID:AB_2491009 9134T; RRID:AB_331589
Anti-mouse STAT3	Cell Signaling Technology	8768S; RRID:AB_2722529
Anti-mouse p-STAT5	Cell Signaling Technology	4322S; RRID:AB_10544692
Anti-mouse STAT5	Cell Signaling Technology	94205T; RRID:AB_2737403
Anti-mouse p-Erk1/2 (Thr202/Tyr204)	Cell Signaling Technology	4370T; RRID:AB_2315112
Anti-mouse Erk1/2	Cell Signaling Technology	4695S; RRID:AB_390779
Anti-mouse beta-actin	Santa Cruz Biotechnology Inc	sc-47778
Anti-human CD1b	Abcam	ab133357; RRID:AB_2650514
Anti-human VISTA	Origene	UM800162CF
Anti-human Pan-cytokeratin	Roche	04015630971268
Anti-human HLA-DR	Invitrogen	14-9956-82
Anti-human ARG1	Cell Signaling Technology	93668; RRID:AB_2800207
TotalSeq B antibody anti-Ly6C	Biologend	28053
TotalSeq B antibody anti-Ly6G	Biologend	127659
TotalSeq B antibody anti-CD11c	Biologend	117359

REAGENT or RESOURCE	SOURCE	IDENTIFIER
Human pan-cytokeratin (AE1/AE3/PCK26)	Roche Diagnostics	05267145001
Human CD11B	Abcam	ab133357; RRID:AB_2650514
Human HLA-DR [LN3]	Invitrogen	14-9956-82
Human VISTA	Origene	UM800162
Human ARG1 [D4E3M]	Cell Signaling Technology	93668; RRID:AB_2800207
Bacterial and virus strains		
NEB [®] 5-alpha Competent E. coli	New England Biolabs	C2987I
Biological samples		
Endometrial tumor tissues	Case Western Reserve University hospital tissue biorepository	N/A
Chemicals, peptides, and recombinant proteins		
Ova 257–264 peptide (SIINFEKL)	Genscript	RP10611
Adpgk peptide HLELASMTNMELMSSIVHQ	Atlantic peptides	Custom synthesis
Rpl18 peptide KAGGKILTFDRLALESPK	Atlantic peptides	Custom synthesis
TRP2 peptide SIYDFVWL	Atlantic peptides	Custom synthesis
Diffluoromethylornithine (DFMO)	Fisher Scientific, Tocris Bioscience [™]	27-611-0
STAT3 inhibitor (Stattic)	Tocris Bioscience Inc	2798
CK2 inhibitor (Silmitasertib)	SelleckChem Inc	CX-4945
Putrescine	Fisher Scientific, MP Biomedicals [™]	ICN10044101
Oligomycin	sigma	CAYM-11342-1
Fluoro-carbonyl cyanide phenylhydrazine	sigma	C2920-10MG
Rotenone	sigma	R8875-1G
Antimycin A	sigma	A8674-50MG
2-deoxy-glucose	sigma	SIAL-D8375-1G
RPMI	ThermoFisher	21870076
GM-CSF	Peprotech	10780-714 (315-03-250ug)
IL-6	Peprotech	216–16
FBS	bio-technie	S11150
HEPES	Life Technologies	15630–080
L-glutamate	ThermoFisher	25030081
2-mercaptoethanol	Sigma	M3148-25ML
Penicillin/streptomycin	Thermo	10378016
Accutase cell detachment medium	Sigma-Aldrich	A6964-100ML
DNase	Sigma	4716728001
Liberase TL	Roche	5401020001
Protease and phosphatase inhibitors	ThermoFisher	78441
Poly-D-Lysine	ThermoFisher	A3890401
MitoTracker [™] Green FM	ThermoFisher	M7514
MitoTracker [™] Deep Red FM	ThermoFisher	M22426
CPGODN 1826	Abeomics	15–1018
Resiquimod R848	Abeomics	15–1016

REAGENT or RESOURCE	SOURCE	IDENTIFIER
Critical commercial assays		
Live/Dead viability dye	ThermoFisher	L34964
MycAlert™ Mycoplasma Detection Kit	Lonza Inc	LT07-418
RNeasy Kit	Qiagen	74004
Foxp3 staining buffer set	Fisher Scientific	00-5521-00
PrimeScript™ 1st strand cDNA Synthesis Kit	Takara	6110B
iTaq™ Universal SYBR® Green Supermix	Bio-Rad	1725121
Seahorse XF cell Mito stress test kit	Agilent	103015-100
EasySep™ Mouse Streptavidin RapidSpheres™ Isolation Kit	Stemcell Tech	19860
Deposited data		
Mouse bulk RNAseq	GEO	GEO: GSE244545
Mouse scRNAseq	GEO	GEO: GSE244797
Experimental models: Cell lines		
MC38	Kerafast	ENH204-FP
B16F10	ATCC	CRL-6475
HEK293T	ATCC	CRL-3216
Experimental models: Organisms/strains		
C57BL/6N (H-2 ^b , CD45.2)	Charles River Laboratories	027
Congenic C57BL/6-Ly5.1	Charles River Laboratories	564
OT-1	JAX	003831
Vsir ^{-/-} mice	(Wang et al., 2014) ¹⁷	(Wang et al., 2014) ¹⁷
Vsir ^{fl/fl} conditional mice	(Yoon et al., 2015) ⁸⁵	(Yoon et al., 2015) ⁸⁵
Cx3r1 .Cre	JAX	025524
Oligonucleotides		
Arg1 forward: ggcaacctgtgtccttctc	Integrated DNA Technologies	N/A
Arg1 reverse: acacgatgtctttggcagat	Integrated DNA Technologies	N/A
inos forward: ccctctgatctgtgttga	Integrated DNA Technologies	N/A
Inos reverse: caaccggagctcctggaac	Integrated DNA Technologies	N/A
Odc1 forward: cgtcattggtgtgagcttcc	Integrated DNA Technologies	N/A
Odc1 reverse: gtatctgcctgctcagcta	Integrated DNA Technologies	N/A
18s forward: aaccggtgaaccatt	Integrated DNA Technologies	N/A
18s reverse: ccaccaatcggtagtagcg	Integrated DNA Technologies	N/A
Recombinant DNA		
STAT3 ^{Y705E} mutant	Wang lab	N/A
STAT3 ^{S727D} mutant	Wang lab	N/A
pBABE-puro	Addgene	1764
FlowJo v 10	FlowJo	N/A
GraphPad	Prism	N/A